Hydration of marginal basins and compositional variations within the continental lithospheric mantle inferred from a new global model of shear and compressional velocity

Andrea Tesoniero, Ludwig Auer, Lapo Boschi, Fabio Cammarano

Hydration of marginal basins and compositional variations within the continental lithospheric mantle inferred from a new global model of shear and compressional velocity.

Andrea Tesoniero[1], Ludwig Auer[2], Lapo Boschi[3,4], and Fabio Cammarano[1]

Corresponding author: Andrea Tesoniero, Department of Geosciences and Natural Resource Management, University of Copenhagen, Øster Voldgade 10, 1350, Copenhagen, Denmark (andrea.tesoniero@ign.ku.dk)

[1]Department of Geosciences and Natural Resource Management, University of Copenhagen, Copenhagen, Denmark

[2]Institut für Geophysik, Eidgenössisch Technische Hochschule, Zürich, Switzerland

[3]Sorbonne Universités, UPMC Univ Paris 06, Institut des Sciences de la Terre Paris (iSTeP), Paris, France

[4]CNRS, Institut des Sciences de la Terre Paris (iSTeP), Paris, France

Abstract. We present a new global model of shear- and compressional wave speeds for the entire mantle, partly based on the dataset employed for the shear-velocity model *savani* [*Auer et al.*, 2014]. We invert Rayleigh and Love surface waves up to the sixth overtone in combination with major P and S body wave phases. Mineral-physics data on the isotropic $\delta lnV_S/\delta lnV_P$ ratio are taken into account in the form of a regularization constraint. The relationship between V_P and V_S that we observe in the top 300 km of the mantle has important thermo-chemical implications. Back-arc basins in the Western Pacific are characterized by large V_P/V_S and not extremely high V_S at ∼150 km depth, consistently with presence of water. Most pronounced anomalies are located in the Sea of Japan, in the back-arc region of the Philippine Sea and in the South China Sea. Our results indicate the effectiveness of slab-related processes to hydrate the mantle and suggest an important role of Pacific plate subduction also for the evolution of the South China Sea. We detect lateral variations in composition within the continental lithospheric mantle. Regions that have been subjected to rifting, collisions and flood basalt events are underlain by relatively large V_P/V_S ratio compared to undeformed Precambrian regions, consistently with a lower degree of chemical depletion. Compositional variations are also observed in deep lithosphere. At ∼200 km depth, mantle beneath Australia and African cratons has comparable positive V_S anomalies with other continental regions, but V_P is ∼1% higher.

1. Introduction

The thermal and chemical structure of the mantle defines its physical properties (i.e., seismic velocities and density) and governs the dynamical evolution of the Earth. Global seismic tomography is a powerful tool to study the deep structure of our planet, but the interpretation of resulting images remains challenging. The intrinsic limitation in what can be resolved by seismic data, on one hand, and trade-off between temperature and compositional effects, on the other, hamper our current knowledge of the Earth's interior. A combined interpretation of data that are sensitive to different physical parameters can help to improve our current understanding of the thermo-chemical mantle structure.

In order to evaluate the relative contribution of temperature (T) and composition (C) in determining the mantle physical properties, especially at long wavelengths and in the deep mantle, joint V_P and V_S inversions have been carried out [e.g., *Robertson and Woodhouse*, 1996; *Su and Dziewonski*, 1997; *Kennett et al.*, 1998; *Masters et al.*, 2000; *Saltzer et al.*, 2001]. A major finding has been an anticorrelation between bulk-sound velocity and shear-wave velocity, which has been interpreted by several authors [e.g., *Trampert et al.*, 2004; *Della Mora et al.*, 2011] as an evidence of chemical anomalies in the lower mantle, although other studies [e.g., *Schuberth et al.*, 2012; *Davies et al.*, 2012] claim that thermal anomalies can equally well reconcile seismic and geodynamical observations.

For the upper mantle, the uneven sampling between P and S structure and the lack of ray coverage make more problematic a joint interpretation of V_P and V_S structure at a global scale. In addition, the effects due to variations in chemical compositions of the upper mantle are secondary to temperature effects [*Cammarano et al.*, 2003; *Afonso et al.*,

2010]. Consequently, it is difficult to detect chemical anomalies by only using seismic data.

Geodynamical observations, such as dynamic topography, tectonic-plate motions and gravity anomalies, provide independent constraints on density (and viscosity) structure and thus help to separate the thermal and chemical anomalies in the Earth's mantle [e.g., *Forte and Perry*, 2000; *Deschamps et al.*, 2002; *Perry et al.*, 2003; *Forte et al.*, 2010; *Simmons et al.*, 2010]. For the upper mantle, these studies confirm the chemical depletion of continental lithosphere and shed a light on possible lateral variations, however resolution is governed by seismic observations.

In general, the interpretation of different geophysical observations relies on knowledge of rocks properties at high pressure and temperature. Most of the knowledge comes from experimental and theoretical mineral physics which studies the elastic and anelastic properties of the Earth's forming materials. Heterogeneity ratios, which relate V_S and V_P variations (i.e. $R_{S/P} = \delta lnV_S/\delta lnV_P$), density to shear-wave velocity variations ($R_{\rho/S} = \delta ln\rho/\delta lnV_S$) and bulk-sound velocity variations to shear-wave velocity variations ($R_{\phi/S} = \delta ln\phi/\delta lnV_S$) have been proposed as diagnostic parameters to separate thermal from compositional anomalies [*Karato*, 1993; *Forte and Perry*, 2000; *Forte and Mitrovica*, 2001; *Perry et al.*, 2003; *Karato and Karki*, 2001; *Cammarano et al.*, 2003; *Forte et al.*, 2010; *Afonso et al.*, 2010].

In this paper, we invert a large seismic dataset to obtain a combined $V_P - V_S$ anisotropic model of the whole mantle. Our model, *SPani*, is an extension of the anisotropic shear-velocity model *savani* [*Auer et al.*, 2014], with the important difference that we also consider datasets sensitive to P-wave structure. Specifically, in addition to the dataset

already used for *savani*, which consists of Rayleigh and Love surface waves up to the sixth overtone measured between periods of 25 to 250s as well as major S-wave phases, we also invert major P-wave phases. A relationship between isotropic V_S and V_P based on mineral physics [*Cammarano et al.*, 2003, 2011; *Karato and Karki*, 2001] is used as an a-priori constraint in the inversion. The isotropic part of our model, and thus V_P/V_S ratios, are not significantly affected by the radial anisotropy structure. We tested that the interpretation of our results does not change even in the case of a purely isotropic inversion.

Although our model extends across the entire mantle, we focus here on a thorough interpretation of the upper mantle structure and leave a more detailed discussion of lower mantle features for future work. In spite of the small sensitivity of Rayleigh waves to V_P, we anticipate that the combination of V_S and V_P in the same model, together with the a-priori mineralogical constraint, provides additional constraints on upper mantle structure, and allows us to identify compositional anomalies in both oceanic and continental regions. Since *Auer et al.* [2014] elaborated extensively about the variations in shear-wave radial anisotropy and our results do not differ significantly from their work, we do not provide a detailed discussion of the anisotropic component of *SPani*. Some of the aspects of the upper mantle radial anisotropy are however presented here.

2. Theoretical background and Data set

We treat the problem of finding the model coefficients that describe the 3D Earth structure in a ray-theory, Jeffreys-Wentzel-Kramers-Brillouin (JWKB) approximation [*Wang and Dahlen*, 1994] and accounting for the effects of lateral variations in the crust as in *Boschi and Ekström* [2002]. The theoretical formulation is the same presented in *Auer*

et al. [2014] and it will not be repeated here. We describe, however, the specific theoretical aspects related to the inclusion of V_P sensitive Rayleigh waves and P-body waves.

2.1. Surface-wave theory

Under the assumption that the Earth constituent material has hexagonal symmetry [*Babuška and Cara*, 1991], in the ray-theory approximation we relate the Love model coefficient A, C, F, L and N [*Love*, 1927] to measurements of phase velocity delay. We convert the Love coefficients into $V_{SV}, V_{SH}, V_{PV}, V_{PH}$, to whom they are related, and we formulate the problem to jointly invert the perturbations for both P- and S- components, while we neglect the effects of density perturbation ρ.

Rayleigh waves are mostly sensitive to shear-velocity perturbations [e.g., *Su and Dziewonski*, 1997; *Ritsema et al.*, 2004]. As a consequence, several authors adopted an approach which ignores the sensitivity of fundamental mode Rayleigh waves and overtones to P-velocity and uses an empirical scaling relationship between V_S and V_P [e.g., *Gung et al.*, 2003; *Panning and Romanowicz*, 2006; *Ritsema et al.*, 2011]. Therefore, resulting V_P models will essentially be scaled versions of the associated V_S model. However, the sensitivity to the V_P upper mantle structure of Rayleigh waves is not entirely negligible, as we show in Figure 1, and it is potentially relevant in defining the upper mantle physical state. In this paper, we explicitly take into account the different sensitivity of Rayleigh waves to V_S and V_P.

2.2. Body-wave theory

We relate the traveltime perturbation of each body-wave phase to the 3D Earth perturbation (i.e. δlnV_{SV}, δlnV_{SH}, δlnV_{PV}, δlnV_{PH}). Most arrival times of P-waves in our

dataset are teleseismic (i.e. epicentral distance of $\sim 25^\circ$ and larger) and the ray trajectories are nearly vertical in the upper mantle, while curving and reaching their bottoming point in the lower mantle (at a depth which is a function of the epicentral distance). P-wave traveltimes provide a good coverage and crossing ray-paths in the lower mantle, where they have been used to produce global models of $3D$ seismic structure [*Dziewonski*, 1984; *Shearer et al.*, 1988; *van der Hilst et al.*, 1997; *Grand et al.*, 1997; *Boschi and Dziewonski*, 2000]. In the upper mantle, the coverage is slightly poorer, and even where the coverage is good, models uniquely based on direct P-wave traveltimes have poor vertical resolution. The effects are twofold: (i) the lateral P-wave heterogeneity structure could be averaged out in regions where there is little or none ray coverage, (ii) in regions with good coverage, the P-wave velocity structure tends to be smeared out in the vertical direction. The vertical smearing can be mitigate with a combination of vertical damping and data weighting of phases sensitive at different depths, which is what we employ in this study.

2.3. Data set

We combine in this study what could possibly be the largest dataset of seismic phases ever used in a global joint seismic tomography. We extend the database of S-body-wave phases, surface waves and overtones used by *Auer et al.* [2014] with ~ 804000 P-arrival times of which more than 600000 are direct minor arc P-phases from *Antolik et al.* [2003]. This database consists of summary rays defined on a $2^\circ \times 2^\circ$ grid and ranging between an epicentral distance of 25° to 100°. Multiple bouncing P-phases are from *Ritsema and van Heijst* [2002].

A list of all the seismic data used in this study is given in Table 1 and Table 2. We

give only details of the P-phases. We refer to *Auer et al.* [2014] for a more detailed description of the employed S-wave phases. We reiterate that P-phases can only resolve upper mantle structure in the proximity of sources and receivers [*Antolik et al.*, 2003]. Due to uneven global coverage of both sources and receivers, the northern hemisphere can be better resolved than the southern one. The resolution drastically improves in the lower mantle, but data coverage remains an issue. For example, in order to increase resolution at the core-mantle boundary (CMB), it is appropriate to include phases which are reflected at (PcP) or crossing (PKP) the CMB [*Boschi and Dziewonski*, 2000]. In this study, we have discarded these phases, since they proved to yield instabilities in the inversion, most likely related to the high uncertainties to which these data are associated with. Multiple bouncing phases such as PP have a strong sensitivity at the bottom of the transition zone and below it, down to 1000-1500 km. Sensitivity to V_S structure gradually becomes dominant in the deeper portion of the mantle (below 1500 km). We rely on the P-sensitivity of Rayleigh surface waves and overtones (compilations by *Ekström* [2011] and *Visser et al.* [2008], respectively) to better resolve the V_P structure in the upper mantle.

2.4. Parameterization

The ability to recover the $3D$ structure of the Earth's interior depends on several factors. Data coverage is probably the most important, but the choices of the reference model, regularization scheme and model parameterization also play a crucial role [*Boschi and Dziewonski*, 1999].

Authors have employed different parameterization schemes and basis functions in which they describe their models. Popular choices include global functions like spherical harmon-

ics [e.g., *Ritsema et al.*, 2011] or local ones, like cubic splines [e.g., *Nettles and Dziewonski*, 2008], spherical sections (i.e. voxels/blocks) [e.g., *Houser et al.*, 2008] or tetrahedra [e.g., *Montelli et al.*, 2004]. Local basis functions provide a better flexibility when dealing with uneven distribution of sources and receivers, which, as denoted earlier, is a problem inherent to any global tomography study. For example, *Auer et al.* [2014] have employed an automatic resampling strategy, which adapts grid density to local ray coverage. This approach is computationally very efficient, but still very expensive if a resolution comparable to that of *Auer et al.* [2014] is to be achieved. In fact, the number of free parameters is roughly doubled by introducing V_P heterogeneity. The problem of defining an adequate parameterization is further complicated by the differences between V_P and V_S coverage. We thus prefer to adopt a regular grid parameterization of $5^\circ \times 5^\circ$ and 28 layers of increasing inter-distance thickness, equivalent to the base grid used by *Auer et al.* [2014]. A regular $5^\circ \times 5^\circ$ grid corresponds almost to a degree-40 spherical-harmonic parameterization and is comparable to the resolution of the previously published joint P and S tomography models.

2.5. On the relationship between V_S and V_P

A number of authors have included a priori relationships between V_S and V_P, based on mineral physics, in joint tomographic inversions of S and P data [*Masters et al.*, 1982; *Ritzwoller et al.*, 1988; *Su and Dziewonski*, 1997; *Masters et al.*, 2000; *Antolik et al.*, 2003; *Houser et al.*, 2008]. Assuming that lateral heterogeneity in the Earth has purely thermal (i.e., not chemical) origin, one can predict a relationship between V_S and V_P heterogeneity based on mineral physics [e.g., *Cammarano et al.*, 2003; *Karato and Karki*, 2001]. $R_{S/P}$ for a reference mantle adiabat (with a potential temperature at 1300°C) is

~ 1.7 throughout the mantle. This value, however, is largely affected by anelastic effects in the upper mantle and thus strongly varies with temperature. For example, at 150 km depth, and for same composition, $R_{S/P}$ is ~ 1.5 in cold regions (mantle adiabat with a potential temperature at 1000°C) and ~ 2.2 in hot regions (1600°C adiabat) [*Cammarano et al.*, 2003]. Effects of anelasticity are less important in the lower mantle. $R_{S/P}$ tends to increase as moving deeper from a reference value of 1.7 (for 1300°C mantle adiabat) at 700 km down to ~ 2.1 at the base of the mantle (our computations agree with *Karato and Karki* [2001] measurements). Although no direct constraints exist, T-dependent anelasticity should again become an important factor closer to the CMB, as T approaches the solidus. Compositional variations and phase transitions significantly complicate the pattern, also introducing non-linear trends with depth.

We propose here a simple depth-dependent scaling scheme based on estimated values from average mantle composition (pyrolite) and a thermal structure given by a 60 m. y. old oceanic lithosphere down to $\sim$ 110 km and a 1300°C mantle adiabat below this depth [*Cammarano et al.*, 2011]. Our $\delta lnV_S/\delta lnV_P$ slightly increases in the top 150 km (from 1.6 to 1.7) and then stays almost constant down to 660 km. It linearly increases in the lower mantle again, reaching a value around 2.1 towards the CMB. We relax the value at the bottom 300 km depths in view of the role of phase-transitions and of the possibility of strong chemical anomalies.

Our a-priori constraint is intentionally chosen as simple as possible and is laterally uniform. This choice is motivated by intrinsic limitations in our approach and on interpretation of seismic data in general. One limitation is related to the very nature of seismic tomography, which is based on perturbation theory. All variations are relative to a reference starting

model, in our case PREM [*Dziewonski and Anderson*, 1981]. In addition, the amplitude of lateral variations also depends on regularization schemes, as previously discussed. The determination of absolute velocities is important to obtain a reliable interpretation of upper mantle structure, where temperature-dependent anelastic effects can be large [e.g., *Karato*, 1993; *Cammarano et al.*, 2003]. The second limitation resides in the poor knowledge of compositional effects on the relationship between V_P and V_S. For instance, in the upper mantle, and for dry compositions, the effect of composition on seismic velocity has been observed to be relatively small compared to that of temperature [*Cammarano et al.*, 2003; *Afonso et al.*, 2010]. However, several residual uncertainties remain, particularly on the role of fluids.

In our inversions, we use a specific value of $R_{S/P}$ at each depth and we accurately test how the applied constraint affects the obtained model and the data fit. We also obtain a model in which we did not apply any scaling relationship between V_S and V_P. The analysis of the V_P structure of this test-model will clarify the need of adding an a-priori constraint to make sure that the outcome of the inversion has a physical meaning.

2.6. Regularization and weighting

Our *joint* inversion of P- and S-sensitive data is implemented by solving:

$$\begin{pmatrix} w_R\mathbf{A}^R_{SV} & 0 & w_R\mathbf{A}^R_{PV} & w_R\mathbf{A}^R_{PH} \\ 0 & w_L\mathbf{A}^L_{SH} & 0 & 0 \\ w_S\mathbf{A}^S_{SV} & w_S\mathbf{A}^S_{SH} & 0 & 0 \\ 0 & 0 & w_P\mathbf{A}^P_{PV} & w_P\mathbf{A}^P_{PH} \\ \lambda\mathbf{D} & 0 & 0 & 0 \\ 0 & \lambda\mathbf{D} & 0 & 0 \\ 0 & 0 & \lambda\mathbf{D} & 0 \\ 0 & 0 & 0 & \lambda\mathbf{D} \\ \gamma\mathbf{I} & 0 & -\gamma R_{S/P}\mathbf{I} & 0 \\ 0 & \gamma\mathbf{I} & 0 & -\gamma R_{S/P}\mathbf{I} \end{pmatrix} \cdot \begin{pmatrix} \mathbf{x}_{SV} \\ \mathbf{x}_{SH} \\ \mathbf{x}_{PV} \\ \mathbf{x}_{PH} \end{pmatrix} = \begin{pmatrix} w_R\mathbf{d}^R \\ w_L\mathbf{d}^L \\ w_S\mathbf{d}^S \\ w_P\mathbf{d}^P \\ 0 \\ 0 \\ 0 \\ 0 \\ 0 \\ 0 \end{pmatrix} \quad (1)$$

The entries of submatrices $\mathbf{A}^R_{SV}$, $\mathbf{A}^R_{PH}$, etc. in eq. (1) are the partial derivatives linking the model parameters $\mathbf{x}_{SV}$, $\mathbf{x}_{PH}$ etc. to the data $\mathbf{d}^R$ etc. Each type of datum (R, L, S, P for Rayleigh, Love, S and P waves, respectively) can be sensitive to a different combination of parameters (SV for vertically polarized shear velocity V_{SV}, etc.). The coefficients w_R, w_L, etc. denote the different weighting factors. The terms $\lambda\mathbf{D}\cdot\mathbf{x}=0$ represent our regularization constraint. A common practice is to choose the operator $\mathbf{D}$ to force the solution to be smooth (roughness damping) [*Boschi and Dziewonski*, 1999, 2000; *Masters et al.*, 2000; *Kustowski et al.*, 2008; *Houser et al.*, 2008]. Other regularization schemes which tend to minimize the difference between the input and the output model (norm damping) could be applied as sole regularization term [*Bijwaard et al.*, 1998; *Clevede et al.*, 2000; *Montelli et al.*, 2004; *Ritsema et al.*, 2004; *Montelli et al.*, 2006] or in combination with the roughness term [*Boschi and Ekström*, 2002; *Nettles and Dziewonski*, 2008]. Here we follow the approach of *Boschi and Dziewonski* [1999] and limit the regularization to the roughness term only: we thus require our solution to be smooth by minimizing the differences in the model parameters between adjacent blocks. The coefficients λ are a measure of the weight applied to the regularization terms. By exploring the effect of different values of λ, we can quantify the impact of the roughness damping on the solution model (discussed in section 3.1).

The two bottom rows appended to the matrix expression (1) represent our mineralogical constraint expressed in the matrix linear form. These terms force the ratio of the inverted model parameters $\delta lnV_{SV}/\delta lnV_{PV}$ and $\delta lnV_{SH}/\delta lnV_{PH}$ to be equal to the mineralogically inferred heterogeneity ratios $R_{S/P}$ presented in section 2.5 and take the form

$$\gamma\frac{\delta lnV_{SV}}{\delta lnV_{PV}} = \gamma\frac{\delta lnV_{SH}}{\delta lnV_{PH}} = \gamma R_{S/P} \tag{2}$$

with a weighting coefficient γ. Therefore, our way of applying mineralogical-based scaling between physical parameters is akin to how we implement the roughness damping in the inversion. The application of regularization schemes in any inverse problem reduces the variance of all the subsets and attenuates the obtained amplitude [*Li and Romanowicz*, 1996; *Mégnin and Romanowicz*, 2000]. We solve the linearized inverse problem by means of a tailored parallel tomography solver based on the $PETSc$ library, which allows us to solve the system using different algorithms. We did not notice any difference between solutions obtained using a parallel implementation of the $LSQR$ algorithm [*Paige and Saunders*, 1982] or the $GMRES$ method [*Saad and Schultz*, 1986]. We present the result in terms of model quality by the analysis of the variance reduction (VR) using the relationship

$$VR = 1 - \frac{\sum_{j=1}^{n}(A_{ij}\cdot x_j) - d_i)^2}{\sum_{i=1}^{m} {d_i}^2} \tag{3}$$

We alternatively calculate variance reduction (i) for the whole data set (cumulative variance reduction), in which case $\mathbf{A}$ in eq. (3) coincides with the matrix at the left-hand side of eq. (1) minus the rows corresponding to regularization (i.e., λ=0, γ=0), or (ii) for any subset of the data (grouped variance reduction), in which case $\mathbf{A}$ is just the portion of matrix associated with a certain type of data, e.g. $\mathbf{A} = (\mathbf{A}^R_{SV}\ , \mathbf{A}^R_{PV}\ , \mathbf{A}^R_{PH})$ for Rayleigh waves. m denotes the number of observations in the subset in question, while n is the number of free parameters, independent of data type.

3. Model result

We present the seismic characteristics of two inverted models. The first represents our preferred joint tomographic model (called *SPani*), the other (called $SPani_{test}$) is a model obtained obtained by selecting $\gamma = 0$ in eq. (1), i.e. without imposing any scaling relationship between V_S and V_P.

We will focus our discussion and interpretation to the isotropic part of our model. We obtain the Voigt average isotropic P and S velocity from our inverted values [e.g., *Panning and Romanowicz*, 2006]:

$$V_P{}^2 = \frac{V_{PV}{}^2 + 4V_{PH}{}^2}{5} \tag{4}$$

$$V_S{}^2 = \frac{2V_{SV}{}^2 + V_{SH}{}^2}{3} \tag{5}$$

3.1. Data fit and model selection

In this study, we opt for the following approach to select our favorite models. (i) We invert our seismic data set using a wide range of weights for the roughness damping parameter λ in eq. (1), and without any further constraint on scaling V_S and V_P variations; (ii) We select our best-fit model, $SPani_{test}$ on the basis of an L-curve analysis [*Hansen*, 1992], (Figure 3) a tool to identify models providing a fair balance between model roughness and data fit; (iii) We run a second set of inversions in which we keep the roughness damping fixed, while changing the weight associated with the scaling ratio $\delta lnV_S/\delta lnV_P$. In one case, we set the weight associated with the scaling term to an extremely high value. This way, we obtain a V_P model that is perfectly scaled to the V_S model. Such a model fits the data well (see Figure 3) and it gives us confidence that our reference mineral physics

constraint is not unrealistic. However, the variance reduction for some subset of data, namely Rayleigh wave overtones, is negative (Figure 4).

Relaxing the mineral physics constraints on $\delta lnV_S/\delta lnV_P$, we are able to obtain a model (*SPani*) that has an improved grouped variance reduction (Figure 4). We will later discuss where and in which way the V_P component of our model differs structurally from the V_S part and draw implications on thermo-chemical structure. A checkerboard resolution test for *SPani* is shown in Supporting Information.

3.2. V_P and V_S Isotropic structure - role of a-priori constraint in the inversion

Most of the differences between *SPani* and $SPani_{test}$ are associated with the V_P component of the joint inverted models. The upper mantle V_P structure of $SPani_{test}$ beneath oceanic regions (Figure 5) is largely uncorrelated with the well-known V_S structure, which is in agreement, to a first order, with the thermal structure of oceanic lithosphere. This result clearly shows the averaging effect of seismic anomalies in the oceanic regions, where the ray coverage is the poorest. Most of the negative V_P anomalies in $SPani_{test}$ are not symmetric with respect of the mid oceanic ridges as they are in the V_S model. In addition, $SPani_{test}$ is characterized by a very strong vertical smearing of structures at the top of the upper mantle into the transition zone. Note, for example, that some of the cratonic roots in $SPani_{test}$ (e.g., Australia) reach 450 km depth. The V_S component of model $SPani_{test}$ resembles very closely the V_S component of our preferred model *SPani*.

In *SPani* (Figure 6 and 7), the a-priori constraint on the relationship between V_S and V_P is able to eliminate the discrepancy in sub-oceanic lithosphere and to reduce the vertical smearing in V_P structure. At the same time, the data fit is very good (Figure 4).

The amplitude of the anomalies are in the order of 5-6% for V_S and 3-4% for V_P models

in the upper mantle and decrease to $\sim$ 1-2%, for both V_S and V_P, in the transition zone and in the lower mantle.

The shear-wave radial anisotropy part of our models closely resembles *savani* and is almost identical to *model A* in *Auer et al.* [2014], a model with the same parameterization we use. Here, we also invert for compressional-wave anisotropy ($\varphi = {V_{PV}}^2/{V_{PH}}^2$), but data resolution does not provide a reliable constraint on φ. Most of the anomalies in $\xi = {V_{SH}}^2/{V_{SV}}^2$ have been already presented in *Auer et al.* [2014] and are not discussed here.

Since most of our interpretation relies on our isotropic V_P and V_S models, we also run a test where we did not model lateral variations in ξ and/or φ. Although lateral variations in ξ appear required by the data, a purely isotropic model will be only slightly affected, not varying the qualitative aspects of our results in terms of V_P/V_S ratio.

4. Model analysis and comparison with other models

In this section, we aim to identify the common features of our joint $V_P - V_S$ tomographic model *SPani* and to quantify the similarities between *SPani* and previously published joint shear-wave and compressional-wave velocity models. We select 3 recent $V_P - V_S$ tomographic models (*PRI-P05 PRI-S05* [*Montelli et al.*, 2004, 2006], *hmsl06* [*Houser et al.*, 2008] and *GyPSuM* [*Simmons et al.*, 2010]). The models are obtained by three different groups and are based on different datasets, parameterization and regularization schemes. We perform a spectral analysis by decomposing the models in spherical harmonics expansions, and we thus compare the models at same spatial wavelength. In order to quantify similarities between the V_S and V_P components of each model, we also measure $V_P - V_S$ correlations between each model.

4.1. Comparison with other $V_P - V_S$ global models

GyPSuM [*Simmons et al.*, 2010] is obtained by a joint inversion of P and S body-wave traveltimes and geodynamical observations, such as free air gravity anomalies, dynamic topography and divergence of the tectonic plates. Including geodynamical observations should provide additional constraints on density, and thus on composition. The model is radially parameterized in 22 layers and blocks of 275×275 km in lateral size i.e. roughly $2.5^\circ \times 2.5^\circ$ degrees.

hmsl06 [*Houser et al.*, 2008] is based on a joint inversion of P- and S-traveltimes and surface-wave fundamental modes. The model is laterally parametrized in blocks of $4^\circ \times 4^\circ$ and 18 vertical layers. The scaling relationship $\delta lnV_S = 1.7\delta lnV_P$ is applied above 660 km depth. No scaling relationship is used below this depth.

Finally, models *PRI-P05* and *PRI-S05* [*Montelli et al.*, 2004, 2006] are obtained by separately inverting P and S body waves arrival times. They are based on finite frequency kernels and parameterized in mesh of tetrahedra with irregular node spacing.

The comparison of *GyPSuM*, *hmsl06* and *PRI* models with *SPani* are shown in Figure 8 for the compressional wave speed component. The overall structural pattern of the V_S models follows that of the compressional ones and the comparison of V_S structure is thus only reported in the supporting information.

All models have been resampled in spherical-harmonics up to 32 degrees. At 150 km depth, all models show the well known ocean-continent dichotomy. The Princeton model, which does neither include surface wave data nor involve mineralogical scaling constraints, is the only one characterized by little structural resolution in the upper mantle, on a global scale. At 350 km depth, the anomalies due to continental lithosphere are not present any-

more, except for *GyPSuM* (Figure 9). In *SPani* and *hmsl06*, we start to see an anomaly that can be associated with the subduction of the Pacific plate. Model *PRI-P05* seems to comprise structures that look like a downward continuation of shallower heterogeneities. The low-velocity anomalies are associated with the South Pacific ridge, the 90E ridge and the East African rift valley. Long wavelength structures start tapering out in the transition zone between 450 km and 650 km. *hmsl06* and *GyPSuM* are more similar to *SPani* in the transition zone as they all exhibit positive velocity anomalies along the circum-pacific ring of fire, while *PRI-P05* is still characterized by channel-like structures. At a depth of 1300 km (Figure 8), all the models consistently image a high-velocity anomaly, which has been associated with the subducted Farallon and Thetian plates [e.g., *van der Hilst et al.*, 1997]. The large degree-2 structure at the CMB is well imaged in all models. The smaller Perm anomaly [*Lekič et al.*, 2012], instead, can only be seen in *SPani* and *GyPSuM*. The V_S models show, overall, similar structure of V_P models.

4.2. Correlation between V_P and V_S structure

We compute the Pearson correlation coefficient (PCC) between the V_P and V_S component of *SPani*, *GyPSuM*, *hmsl06* and *PRI*, by considering the original models and smoothed versions, resampled at different spatial wavelengths: i.e. up to harmonic degree 8, 12, 24 and 32 (Figure 9). The models show the highest $V_P - V_S$ correlation at long wavelengths [*Becker and Boschi*, 2002]. Seismic models that include surface-wave data (i.e, *SPani* and *hmsl06*) are characterized by a particularly high correlation in the top part of the mantle. *SPani* V_P and V_S correlate up to 90% in the first 300-350 km for all harmonics expansions (Figure 9). This is most likely due to the resolution supplied by surface waves and overtones, and possibly to the imposed relationship between the V_S

and V_P model. Similarly to *SPani*, *hmsl06* has a very high-value correlation coefficient, (95%) in the upper mantle.

The correlation coefficient between V_P and V_S in *SPani* significantly decreases in the transition zone, where the seismic structure is also less well resolved. This is not the case for *hmsl06*, which maintains a very high $V_P - V_S$ correlation ($\sim 90\%$) down to the bottom of the transition zone (Figure 9). The difference between V_P and V_S structure for *hmsl06* starts to become relevant only below 650 km depth, where the scaling relationship between δlnV_S and δlnV_P is no longer imposed. *GyPSum* also shows an overall high correlation ($\sim 90\%$) throughout the upper mantle, but it is characterized by a peculiar alternating trend and almost no differences in the correlation coefficient at the different spherical-harmonics expansions (Figure 9). The coupling between geophysical and geodynamical observations, which also requires a viscosity profile, can be a possible cause for the observed behavior. Finally, the Princeton models show a pattern similar to *hmsl06*, and are also characterized by high correlation in the upper mantle. *PRI-P05* and *PRI-S05* are based on separate inversions and, more importantly, include only body waves data. The *PRI* models also show larger variations between correlations referring to models resampled at different spatial wavelengths (Figure 9).

In the lower mantle, the correlation between the different models is overall smaller than in the upper mantle. The correlation coefficient reaches minimum values $\sim 55\%$ for *PRI* and *hmsl06*, but the values goes up to 65-70% when only the long wavelength components of these models are considered. After a minimum in the transition zone, the correlation associated with *SPani* grows again to $\sim 70\%$. *GyPSum* reaches an overall higher correlation than the other models (with a minimum of 80% at ~ 2000 km depth). Interestingly,

the depth in which the models reach their maximum $V_P - V_S$ correlation is variable. *SPani* has a maximum value at 2500 km, in agreement with a weak relationship imposed between V_P and V_S near the CMB and with the absence of CMB sensitive phases. Also *hmsl06* peaks at same depth, while *PRI* and *GyPSum* have their best $V_P - V_S$ correlation close to the CMB.

In summary, the proposed $V_P - V_S$ joint models show the highest correlation in the upper mantle and, more importantly, different models are characterized by different correlation-depth patterns, which seem to depend on the employed data sets and regularization schemes.

5. Structural variations between V_P and V_S and V_P/V_S ratio

The combination of V_P and V_S sensitive data in a joint inversion allows us to investigate the differences between the V_S and V_P parts of the model by means of the V_P/V_S ratio. Because of the uncertainties related to the absolute velocities, the interpretation of the amplitude of the V_P/V_S ratio can be misleading [e.g., *Afonso et al.*, 2010]. Nevertheless, relative lateral variations in V_P/V_S ratio are very valuable for interpretation and are shown in Figure 10 for four upper mantle depths.

The structural pattern depicted in these maps follows that of Figures 6 and 7, but with some important additions. In the top 200 km the most striking feature is the dichotomy oceans-continents, with oceans showing high values in the V_P/V_S ratio and low values in continental regions. A peculiar anomaly is localized in the Western Pacific margin, where the highest V_P/V_S values are recorded (Figure 10). It is important to note that the V_P/V_S ratio in this area is higher than what we observe at the mid-ocean ridges, where the lowest velocities are found (see for example relative V_S variations at 150 km depth in Figure 7).

We have carried out extensive synthetic tests to ensure that the isotropic V_P/V_S ratio is not contaminated by the anisotropic component of our model. One of such tests consists in allowing only isotropic variations, and gave a model with very similar V_P/V_S ratios. Moreover, the anomaly is already present at long wavelength (for example in a version of the model resampled up to spherical harmonics degree 18, in Supporting Information). We conclude that the Western Pacific anomaly is a robust feature of our joint tomographic inversion.

Below $\sim$ 250 km, the distribution in V_P/V_S ratio becomes less heterogeneous and most of the ocean-continent dichotomy starts to disappear. Nevertheless, it is still possible to observe low V_P/V_S ratios beneath the North-America craton and the Baltic shield. Anomalies related to subducting slabs become dominant below 250 km depth. It is possible to observe, for example, the signature of the subducting slab in the Western Pacific at a depth of $\sim$350 km.

6. Discussion and interpretation

Any decorrelation between V_S and V_P structure may be indicative of a possible compositional effect. In addition, V_P/V_S ratio can be also a useful factor for thermo-chemical interpretation. Estimated V_P/V_S values based on mineral physics seem to suggest a weak sensitivity to changes in dry composition [*Cammarano et al.*, 2003; *Afonso et al.*, 2010], particularly in relation with the larger compositional effect on the density-V_S heterogeneity ratio. Several questions remain about the role of fluids and melts in determining the V_P/V_S ratio. The ratio between V_P and V_S has been used as an indicator of compositional heterogeneity in the continental crust and lithospheric mantle [*Lee*, 2003; *Niu et al.*, 2004; *Chou et al.*, 2009]. The effects of adding water on seismic velocities at high pressure is not

yet well quantified, but the qualitative aspects suggest an increase in the V_P/V_S ratio. A water-rich region can be characterized by a strong reduction in V_S and a less strong effect on V_P (mostly due to anelastic effects and/or induced partial melt [*Karato*, 2004]), therefore increasing the V_P/V_S ratio compared to dry regions [e.g., *Dinc et al.*, 2011; *Kamiya and Kobayashi*, 2000].

Even in the case of a perfectly known compositional effect on V_P/V_S ratio, we should recap the limitation of any tomographic seismic model in recovering absolute velocities, and thus in determining V_P/V_S ratios. Assuming only thermal lateral variations, colder regions should be characterized by higher seismic velocities and the scaling between V_S and V_P should roughly follow our mineral physics based relationship. The opposite is true for regions that are relatively hot, although partial melt or temperature-dependent anelastic effects determine a sensible deviation of the V_P/V_S ratio toward higher values. In our inversion, we apply the same $\delta lnV_S/\delta lnV_P$ at a given depth. If the scaling between V_P and V_S exactly follows our a-priori educated guess, we expect a linear trend with a decrease in V_P/V_S ratio in low-velocity regions and an increase in relatively faster regions. Note that this effect, also observed in our model (Figure 10), is mostly due to the relation between V_P/V_S ratio and absolute velocities. For example, at $V_P = 8km/s$ and $V_S = 4.444km/s$ (i.e. $V_P/V_S = 1.8$) (values roughly corresponding to reference velocities at 150 km), the V_P/V_S ratio will range between 1.66 and 1.95 for a $\pm 3\%$ V_P variation, if $\delta lnV_S/\delta lnV_P = 1.7$.

In Figure 11, we show the relative percent variations of *SPani* V_P structure from a perfectly scaled V_P structure the top 350 km of the mantle. The perfectly scaled V_P structure has been estimated on the basis of the used used $\delta lnV_S/\delta lnV_P$.

6.1. Evidence of hydration of Asian marginal basins

At 150 km depth, the obtained V_P (and thus V_P/V_S ratio) is almost 2% higher than expected in a very large area, which includes the Philippine Sea, the South China Sea and the Sea of Japan. A close up of the regions together with surface features from the plate boundary model *PB2002* [*Bird*, 2003] is shown in Figure 12.

This anomalous area is located in a very complicated tectonic region, surrounded by subducting slabs, and in correspondence of two main tectonic plates, i.e. the Philippine Sea plate and the Sunda plate. Several smaller plates, mostly limited by convergent margins, are also involved . We notice the presence of robust, large-scale anomalies.

All the anomalies are located in back-arc basins that experienced an extension due to roll back of subducting slabs. The Philippine Sea anomaly is centered, at 100 km depth, in the largest back-arc basin in the world (the Parece-Vela basin) and does not extend westward beyond the remnant arc, the Kyushu-Palau Ridge (Figure 12, panel a). At larger depth, the core of this anomaly is observed at the south border of the Philippine Sea, entering the Caroline Plate (Figure 12, panel 150 km and 200 km). A second anomaly is elongated and located in the Sea of Japan. The anomaly tapers out at $\sim$ 200 km depth (Figure 12, panel c). The third anomaly is located in the South China Sea and becomes stronger between 150 and 200 km (Figure 12). All the anomalies fade away beneath 250 km depth.

The Philippine Sea anomaly is associated with back-arc spreading due to rapid retreating of the Mariana subduction in a period between $\sim$ 35 Ma to $\sim$ 15 Ma [e.g., *Sdrolias et al.*, 2004]. A rapid retreating regime is consistent with strong weakening of the overriding plate by both fluids and melts [*Baitsch-Ghirardello et al.*, 2014]. The evolution of the two other back-arc basins is more controversial. The Himalayan continental collision could

have been an important role in the formation and evolution of the South China Sea [e.g. *Tapponnier et al.*, 1982]. To some extent, even the Japan Sea may have been affected [e.g., *Jolivet et al.*, 1994]. The formation of these two basins is contemporaneous to the Parece-Vela Basin, suggesting that subduction of western Pacific also played a role. For example, *Fournier et al.* [2004] proposed that the South China Sea is a back-arc basin having an axisymmetric spreading that is governed by the large-scale strike slip shear zones driven by the collision of the India Plate with the Eurasian continent. A similar structural control from tectonic lineaments due to the Himalaya collision has been proposed by *Jolivet et al.* [1994] also for the Sea of Japan.

The detection of similar anomalies in the three regions confirms the importance of subduction related processes in determining the evolution of Asian marginal basins. The zones marked by positive anomalies (red) correspond to places where our model requires V_P to be as much as 2% higher than the expected value, whereas the shear velocity remains low. The existence of such a strong anomaly suggests that the water released by the subducting slabs is not easily outgassed, but remains in the mantle, affecting its physical properties. We thus conclude that the presence of water is responsible for the detected seismic signature. The effectiveness of subduction-related processes in modifying the physical properties of plate surrounded by active convergent margins, such as the Philippine and Sunda plates, has important geodynamical implications [e.g., *Faccenna et al.*, 2004; *van Keken*, 2003; *Le Voci et al.*, 2014]. For example, dehydration in the slab, mostly active in the top 200 km [*Schmidt and Poli*, 1998] can alter the rheological properties of the back-arc region and small-scale convection can be facilitated [*Le Voci et al.*, 2014].

6.2. Variations in chemical depletion of the continental lithosphere

Large parts of continental regions have remained largely undeformed for more than 2.5 billion years. Petrological and geophysical constraints [e.g., *Jordan*, 1975, 1978; *Forte and Perry*, 2000] indicate that the continental lithosphere, i.e. the rigid outer layer that includes the crust ($\sim$ 30 km) and the uppermost mantle, is thick, cold and is chemically distinct (strongly melt-depleted in composition) compared to the oceanic lithosphere. The chemical buoyancy is able to balance the thermal effects on density, thus reconciling the observation of seismically fast (cold) lithosphere and the absence of geoid and gravity anomalies beneath old continental regions.

The basic concept of the thermo-chemical layer underlaying old continental regions (named tectosphere by *Jordan* [1975]) is well accepted and confirmed by many studies, but several open questions remain on the exact compositional nature of the lithosphere, on its depth extent and on the lateral variations both in composition than in (thermal) lithosphere-astenosphere-boundary [*Gung et al.*, 2003; *Artemieva*, 2006; *Griffin et al.*, 2009; *Yuan et al.*, 2011]. For example, the average composition of Archean lithospheric mantle, as inferred by petrological studies, is not consistent with geophysical observations and suggests that the deeper part of the lithospheric mantle is less depleted due to metasomatic processes [*Griffin et al.*, 2009].

In general, seismic studies of reflected and converted phases [e.g., *Rychert et al.*, 2005; *Fischer et al.*, 2010], long-range seismic profiles [e.g., *Thybo and Perchuć*, 1997] and high-resolution tomography [e.g., *Yuan et al.*, 2011; *Porritt et al.*, 2014] indicate a large degree of lateral and vertical variability within the continental lithosphere.

The combination of $P-$ and $S-$wave sensitive data into a joint $V_P - V_S$ inversion allows

us to improve horizontal resolution compared to global V_S models in well-sampled continental regions. Unfortunately, most of the continents remain poorly covered, but our model has some interesting features that deserve further discussion.

In general, *SPani* is characterized by low V_S and V_P/V_S values corresponding to old continental regions (Figure 13 and Figure 10 for V_P/V_S) down to a depth of $\sim$ 250 km. At $\sim$150 km depth, the extension of low V_S covers most of the shield and platform areas around the globe. At 250 km depth (Figure 13, left-bottom panel), our model still shows strong anomalies, mostly in correspondence of Archean and Proterozoic regions: East European craton, North American craton, central Australia, African cratonic blocks and Antarctica (the latter only shown in Figure 10). The results are in substantial agreement with previously published tomography models. Note that the low V_P/V_S are mostly due to the high V_S and, as discussed earlier, are not well constrained by tomography.

It is useful to analyze the decorrelation between the V_P and V_S components of our model (Figure 13, right panels). At 150 km depth, the V_S model does not allow to identify any lateral variation under extremely large continental regions. However, the V_P component of our model shows distinct structural variations.

In the East European craton, the lithospheric mantle below the oldest part of the Baltic Shield, i.e the Kola-Karenian cratons, is well separated from the Russian platform to the East (Figure 13, right panels). The positive anomaly is in agreement with the hypothesis of a more fertile Russian platform, probably owing to metasomatic processes [*Artemieva*, 2003]. The anomaly extends at least down to 250 km, also in agreement with the large values of lithospheric thickness inferred from independent studies [e.g., *Artemieva and Mooney*, 2001]. At 150 km depth, a distinct anomaly corresponding to Sveco-Norwegian

craton ($\sim 1.0 - 1.3$ G.a., [*Artemieva*, 2003]) also emerges.

The Central Australia and African cratonic blocks are characterized by low V_S down to $\sim$ 250 km, but they loose any anomalous structural variation between V_P and V_S below $\sim$ 200 km (Figure 13). Again, this result can be associated with large compositional variations between continents, probably due to a variable degree of metasomatism in the deeper part of the continental lithosphere.

The Siberian craton anomaly is not a strong feature in our model, consistently with what observed in previous global models. In spite of poor seismic coverage in Siberia, we note that the V_S anomaly at $\sim$ 200 km depth is located in the western part of the craton, an area interested by extensive basalts outcrops (place of the Siberian traps, a large igneous province formed $\sim$ 250 M.a. ago) and tectonically separated from the eastern part of the Siberian craton [e.g., *Rosen et al.*, 1994], while the anomalously low V_P/V_S ratio is shifted toward east (Figure 13). The difference can be explained by compositional variations, with a relatively more depleted average composition beneath the eastern blocks of the Siberian craton.

Finally, beneath the North America craton, we also observe distinct structural variations (Figure 13) that extend down to $\sim$ 250 km depth. In correspondence of the Trans-Hudsonian Suture Zone, we observe a relatively high V_P/V_S ratio. A similar lineament, which includes the Keweenawan Rift in the South part, but also part of the Superior craton is observed along 90W meridian. While the anomaly related to Trans-Hudson collision can be explained by compositional variations, the interpretation of the second anomaly is more problematic. According to our model, the south part of the lithospheric mantle below the Superior craton is, on average, chemically different from the rest of the

craton. We note that the more fertile region of Superior includes large igneous provinces (Animikie and MacKenzie dykes).

7. Conclusions

We derive a new joint $V_P - V_S$ tomographic model by inverting a large dataset of surface waves and overtones phase delay measurements as well as traveltime delay of major P- and S- body wave phases. Our model resolves structural anomalies in the ratio between V_P and V_S that have important implications for the thermo-chemical structure of the upper mantle.

Marginal basins in the Western Pacific are characterized by the highest V_P/V_S ratio worldwide and, at the same time, by not extremely low δlnV_S. This feature suggests that hydration due to slab dynamics was an important governing factor in the course of their evolution. The similarity of the anomalies beneath the intra-oceanic back-arc basin of the Philippine Sea and the South China Sea indicates that the Pacific plate subduction played an important role also in the evolution of the South China Sea. The effectiveness of slab-related processes to hydrate large portions of mantle can have strong implications on plate dynamics at a global scale and it gives a new insight on the net flux of water in the Earth's interior. Within continental regions, the analysis of our model suggests the presence of large-scale compositional variations. Regions interested by past rifting, collisions and outcropping of large igneous provinces are generally more enriched than undeformed Precambrian areas. This result is in agreement with enhanced metasomatic processes in those regions. Metasomatic processes can be also responsible for the disappearance of chemical heterogeneity below $\sim$ 200 km in deep ($\sim$ 300 km, according to our model) continental lithospheric mantle in Africa and Australia.

Acknowledgments. We thank the various authors for making their data available. The 3D velocity model is available upon request to the main author (andrea.tesoniero@ign.ku.dk). The code used to solve the seismic inverse problem can be downloaded from https://github.com/auerl/petscinv. This work is supported by Danish Research Council, Sapere Aude grant n. 11-105974.

References

Afonso, J. C., G. Ranalli, M. Fernàndez, W. L. Griffin, S. Y. O'Reilly, and U. Faul (2010), On the Vp/Vs-Mg# correlation in mantle peridotites: Implications for the identification of thermal and compositional anomalies in the upper mantle, *Earth and Planetary Science Letters*, *289*(3-4), 606–618, doi:10.1016/j.epsl.2009.12.005.

Antolik, M., Y. J. Gu, G. Ekström, and A. M. Dziewonski (2003), J362D28: a new joint model of compressional and shear velocity in the Earth's mantle, *Geophysical Journal International*, *153*(2), 443–466, doi:10.1046/j.1365-246X.2003.01910.x.

Artemieva, I. M. (2003), Lithospheric structure, composition, and thermal regime of the East European Craton: implications for the subsidence of the Russian platform, *Earth and Planetary Science Letters*, *213*(3-4), 431–446, doi:10.1016/S0012-821X(03)00327-3.

Artemieva, I. M. (2006), Global $1^\circ \times 1^\circ$ thermal model TC1 for the continental lithosphere: Implications for lithosphere secular evolution, *Tectonophysics*, *416*(1-4), 245–277, doi:10.1016/j.tecto.2005.11.022.

Artemieva, I. M., and W. D. Mooney (2001), Thermal thickness and evolution of Precambrian lithosphere: A global study, *Journal of Geophysical Research: Solid Earth*, *106*(B8), 16,387–16,414, doi:10.1029/2000JB900439.

607 Auer, L., L. Boschi, T. W. Becker, T. Nissen-Meyer, and D. Giardini (2014), Savani: A
608 variable resolution whole-mantle model of anisotropic shear velocity variations based on
609 multiple data sets, *Journal of Geophysical Research: Solid Earth*, *119*(4), 3006–3034,
610 doi:10.1002/2013JB010773.

611 Babuška, V., and M. Cara (1991), *Seismic Anisotropy in the Earth*, 219 pp., Springer.

612 Baitsch-Ghirardello, B., T. V. Gerya, and J.-P. Burg (2014), Geodynamic regimes of intra-
613 oceanic subduction: Implications for arc extension vs. shortening processes, *Gondwana*
614 *Research*, *25*(2), 546–560, doi:10.1016/j.gr.2012.11.003.

615 Becker, T. W., and L. Boschi (2002), A comparison of tomographic and geodynamic
616 mantle models, *Geochemistry, Geophysics, Geosystems*, *3*(1), 2001GC000,168, doi:
617 10.1029/2001GC000168.

618 Bijwaard, H., W. Spakman, and E. R. Engdahl (1998), Closing the gap between regional
619 and global travel time tomography, *Journal of Geophysical Research: Solid Earth*, *103*,
620 30,055–30,078, doi:10.1029/98JB02467.

621 Bird, P. (2003), An updated digital model of plate boundaries, *Geochemistry, Geophysics,*
622 *Geosystems*, *4*(3), 1027, doi:10.1029/2001GC000252.

623 Boschi, L., and A. M. Dziewonski (1999), High- and low-resolution images of the earth's
624 mantle: Implications of different approaches to tomographic modeling, *Journal of Geo-*
625 *physical Research: Solid Earth*, *104*(B11), 25,567–25,594, doi:10.1029/1999JB900166.

626 Boschi, L., and A. M. Dziewonski (2000), Whole earth tomography from delay times of
627 P, PcP, and PKP phases: Lateral heterogeneities in the outer core or radial anisotropy
628 in the mantle?, *Journal of Geophysical Research: Solid Earth*, *105*(B6), 13,675–13,696,
629 doi:10.1029/2000JB900059.

Boschi, L., and G. Ekström (2002), New images of the Earth's upper mantle from measurements of surface wave phase velocity anomalies, *Journal of Geophysical Research*, *107*(B4), 2059, doi:10.1029/2000JB000059.

Cammarano, F., S. Goes, P. Vacher, and D. Giardini (2003), Inferring upper-mantle temperatures from seismic velocities, *Physics of the Earth and Planetary Interior*, *138*(3-4), 197–222, doi:10.1016/S0031-9201(03)00156-0.

Cammarano, F., P. Tackley, and L. Boschi (2011), Seismic, petrological and geodynamical constraints on thermal and compositional structure of the upper mantle: global thermochemical models, *Geophysical Journal International*, *187*(3), 1301–1318, doi:10.1111/j.1365-246X.2011.05223.x.

Chou, H.-C., B.-Y. Kuo, L.-Y. Chiao, D. Zhao, and S.-H. Hung (2009), Tomography of the westernmost Ryukyu subduction zone and the serpentinization of the fore-arc mantle, *Journal of Geophysical Research: Solid Earth*, *114*(B12), doi:10.1029/2008JB006192.

Clevede, E., C. Mégnin, B. Romanowicz, and P. Lognonne (2000), Seismic waveform modeling and surface wave tomography in a three-dimensional Earth: asymptotic and non-asymptotic approaches, *Physics of the Earth and Planetary Interiors*, *119*(1-2), 3756, doi:10.1016/S0031-9201(99)00152-1.

Dahlen, F. A., and J. Tromp (1998), *Theoretical Global Seismology*, Princeton.

Davies, D. R., S. Goes, J. Davies, B. Schuberth, H.-P. Bunge, and J. Ritsema (2012), Reconciling dynamic and seismic models of Earth's lower mantle: The dominant role of thermal heterogeneity, *Earth and Planetary Science Letters*, *353-354*(0), 253–269, doi:10.1016/j.epsl.2012.08.016.

652 Della Mora, S., L. Boschi, P. J. Tackley, T. Nakagawa, and D. Giardini (2011), Low seismic
653 resolution cannot explain S/P decorrelation in the lower mantle, *Geophysical Research*
654 *Letters*, *38*(12), L12,303, doi:10.1029/2011GL047559.

655 Deschamps, F., J. Trampert, and R. Snieder (2002), Anomalies of temperature and
656 iron in the uppermost mantle inferred from gravity data and tomographic models,
657 *Physics of the Earth and Planetary Interiors*, *129*(3-4), 245–264, doi:10.1016/S0031-
658 9201(01)00294-1.

659 Dinc, A. N., W. Rabbel, E. R. Flueh, and W. Taylor (2011), Mantle wedge hydration
660 in Nicaragua from local earthquake tomography, *Geophysical Journal International*,
661 *186*(1), 99–112, doi:10.1111/j.1365-246X.2011.05041.x.

662 Dziewonski, A. M. (1984), Mapping the lower mantle: Determination of lateral hetero-
663 geneity in P velocity up to degree and order 6, *Journal of Geophysical Research: Solid*
664 *Earth*, *89*(B7), 5929–5952, doi:10.1029/JB089iB07p05929.

665 Dziewonski, A. M., and D. L. Anderson (1981), Preliminary reference Earth model,
666 *Physics of the Earth and Planetary Interiors*, *25*(4), 297–356, doi:10.1016/0031-
667 9201(81)90046-7.

668 Ekström, G. (2011), A global model of Love and Rayleigh surface wave dispersion
669 and anisotropy, 25-250 s, *Geophysical Journal International*, *187*(3), 1668–1686, doi:
670 10.1111/j.1365-246X.2011.05225.x.

671 Faccenna, C., C. Piromallo, A. Crespo-Blanc, L. Jolivet, and F. Rossetti (2004), Lateral
672 slab deformation and the origin of the western Mediterranean arcs, *Tectonics*, *23*(1),
673 TC1012, doi:10.1029/2002TC001488.

674 Faure, S. (2006), World kimberlites consorem database version 2006-2.

675 Fischer, K. M., H. A. Ford, D. L. Abt, and C. A. Rychert (2010), The lithosphere-
676 asthenosphere boundary, *Annual Review of Earth and Planetary Sciences*, *38*(1), 551–
677 575, doi:10.1146/annurev-earth-040809-152438.

678 Forte, A. M., and J. X. Mitrovica (2001), Deep-mantle high-viscosity flow and thermo-
679 chemical structure inferred from seismic and geodynamic data, *Nature*, *410*, 1049–1056,
680 doi:10.1038/35074000.

681 Forte, A. M., and H. K. C. Perry (2000), Geodynamic evidence for a chem-
682 ically depleted continental tectosphere, *Science*, *290*(5498), 1940–1944, doi:
683 10.1126/science.290.5498.1940.

684 Forte, A. M., S. Qur, R. M. N. A. Simmons, S. P. Grand, J. X. Mitrovica, and D. B. Rowley
685 (2010), Joint seismic-geodynamic-mineral physical modelling of African geodynamics:
686 A reconciliation of deep-mantle convection with surface geophysical constraints, *Earth*
687 *and Planetary Science Letters*, *295*(3-4), 329–341, doi:10.1016/j.epsl.2010.03.017.

688 Foulger, G. R., G. F. Panza, I. M. Artemieva, I. D. Bastow, F. Cammarano, J. R. Evans,
689 W. B. Hamilton, B. R. Julian, M. Lustrino, H. Thybo, and T. B. Yanovskaya (2013),
690 Caveats on tomographic images, *Terra Nova*, *25*(4), 259–281, doi:10.1111/ter.12041.

691 Fournier, M., L. Jolivet, P. Davy, and J.-C. Thomas (2004), Backarc extension and colli-
692 sion: an experimental approach to the tectonics of Asia, *Geophysical Journal Interna-*
693 *tional*, *157*(2), 871–889, doi:10.1111/j.1365-246X.2004.02223.x.

694 Grand, S. P., R. D. van der Hilst, and S. Widiyantoro (1997), Global seismic tomography:
695 A snapshot of convection in the earth, *GSA today*, *7*, 1–7.

696 Griffin, W. L., S. Y. O'Reilly, J. C. Afonso, and G. C. Begg (2009), The composition and
697 evolution of lithospheric mantle: a re-evaluation and its tectonic implications, *Journal*

of Petrology, *50*(7), 1185–1204, doi:10.1093/petrology/egn033.

Gung, Y., M. Panning, and B. Romanowicz (2003), Global anisotropy and the thickness of continents, *Nature*, *422*, 707–710, doi:10.1038/nature01559.

Hansen, P. C. (1992), Analysis of discrete ill-posed problems by means of the L-Curve, *SIAM Review, Society for Industrial and Applied Mathematics*, *34*, 561–580.

Houser, C., G. Masters, P. Shearer, and G. Laske (2008), Shear and compressional velocity models of the mantle from cluster analysis of long-period waveforms, *Geophysical Journal International*, *174*(1), 195–212, doi:10.1111/j.1365-246X.2008.03763.x.

Jolivet, L., K. Tamaki, and M. Fournier (1994), Japan Sea, opening history and mechanism: A synthesis, *Journal of Geophysical Research: Solid Earth*, *99*(B11), 22,237–22,259, doi:10.1029/93JB03463.

Jordan, T. H. (1975), The continental tectosphere, *Reviews of Geophysics*, *13*(3), 1–12, doi:10.1029/RG013i003p00001.

Jordan, T. H. (1978), Composition and development of the continental tectosphere, *Nature*, *274*(5671), 544–548, doi:10.1038/274544a0.

Kamiya, S., and Y. Kobayashi (2000), Seismological evidence for the existence of serpentinized wedge mantle, *Geophysical Research Letters*, *27*(6), 819–822, doi:10.1029/1999GL011080.

Karato, S. (1993), Importance of anelasticity in the interpretation of seismic tomography, *Geophysical Research Letters*, *20*(15), 1623–1626, doi:10.1029/93GL01767.

Karato, S., and B. B. Karki (2001), Origin of lateral variation of seismic wave velocities and density in the deep mantle, *Journal of Geophysical Research: Solid Earth*, *106*(B10), 21,771–21,783, doi:10.1029/2001JB000214.

721 Karato, S.-I. (2004), *Inside the Subduction Factory*, chap. Mapping Water Content in
722 the Upper Mantle, pp. 138–151, American Geophysical Union, Washington, D. C, doi:
723 10.1029/138GM08.

724 Kennett, B. L. N., S. Widiyantoro, and R. D. van der Hilst (1998), Joint seismic tomogra-
725 phy for bulk sound and shear wave speed in the Earth's mantle, *Journal of Geophysical*
726 *Research: Solid Earth*, *103*(B6), 12,469–12,493, doi:10.1029/98JB00150.

727 Kustowski, B., G. Ekström, and A. M. Dziewonski (2008), Anisotropic shear-wave velocity
728 structure of the Earths mantle: A global model, *Journal of Geophysical Research: Solid*
729 *Earth*, *113*(B6), doi:10.1029/2007JB005169.

730 Le Voci, G., D. R. Davies, S. Goes, S. C. Kramer, and C. R. Wilson (2014), A systematic
731 2-D investigation into the mantle wedge's transient flow regime and thermal structure:
732 Complexities arising from a hydrated rheology and thermal buoyancy, *Geochemistry,*
733 *Geophysics, Geosystems*, *15*(1), 28–51, doi:10.1002/2013GC005022.

734 Lee, C.-T. A. (2003), Compositional variation of density and seismic velocities in natural
735 peridotites at STP conditions: Implications for seismic imaging of compositional hetero-
736 geneities in the upper mantle, *Journal of Geophysical Research: Solid Earth*, *108*(B9),
737 doi:10.1029/2003JB002413.

738 Lekič, V., S. Cottaar, A. Dziewonski, and B. Romanowicz (2012), Cluster analysis
739 of global lower mantle tomography: A new class of structure and implications for
740 chemical heterogeneity, *Earth and Planetary Science Letters*, *357-358*(0), 68–77, doi:
741 http://dx.doi.org/10.1016/j.epsl.2012.09.014.

742 Li, X.-D., and B. Romanowicz (1996), Global mantle shear velocity model developed
743 using nonlinear asymptotic coupling theory, *Journal of Geophysical Research*, *101*(B10),

744 22,245–22,273, doi:10.1029/96JB01306.

745 Love, A. E. H. (1927), *A Treatise on the Mathematical Theory of Elasticity*, Cambridge
746 Univ. Press, Cambridge, reprinted in 1944 by Dover Publications.

747 Masters, G., T. H. Jordan, P. G. Silver, and F. Gilbert (1982), Aspherical Earth structure
748 from fundamental spheroidal-mode data, *Nature*, *298*, 609–613, doi:10.1038/298609a0.

749 Masters, G., G. Laske, H. Bolton, and A. Dziewonski (2000), *The Relative Behavior of*
750 *Shear Velocity, Bulk Sound Speed, and Compressional Velocity in the Mantle: Implica-*
751 *tions for Chemical and Thermal Structure*, chap. 3, pp. 63–87, American Geophysical
752 Union, doi:10.1029/GM117p0063.

753 Mégnin, C., and B. Romanowicz (2000), The three-dimensional shear velocity structure of
754 the mantle from the inversion of body, surface and higher-mode waveforms, *Geophysical*
755 *Journal International*, *143*(3), 709–728, doi:10.1046/j.1365-246X.2000.00298.x.

756 Montelli, R., G. Nolet, F. A. Dahlen, G. Masters, E. R. Engdahl, and S.-H. Hung
757 (2004), Finite-frequency tomography reveals a variety of plumes in the mantle, *Sci-*
758 *ence*, *303*(5656), 338–343, doi:10.1126/science.1092485.

759 Montelli, R., G. Nolet, F. A. Dahlen, and G. Masters (2006), A catalogue of deep man-
760 tle plumes: New results from finite-frequency tomography, *Geochemistry, Geophysics,*
761 *Geosystems*, *7*(11), doi:10.1029/2006GC001248.

762 Nettles, M., and A. M. Dziewonski (2008), Radially anisotropic shear velocity structure of
763 the upper mantle globally and beneath North America, *Journal of Geophysical Research:*
764 *Solid Earth*, *113*(B2), doi:10.1029/2006JB004819.

765 Niu, F., A. Levander, C. M. Cooper, C.-T. A. Lee, A. Lenardic, and D. E. James
766 (2004), Seismic constraints on the depth and composition of the mantle keel beneath

the Kaapvaal craton, *Earth and Planetary Science Letters*, *224*(3-4), 337–346, doi: 10.1016/j.epsl.2004.05.011.

Paige, C. C., and M. A. Saunders (1982), LSQR: An algorithm for sparse linear equations and sparse least squares, *ACM Transactions on Mathematical Software (TOMS)*, *8*, 43–71, doi:10.1145/355984.355989.

Panning, M., and B. Romanowicz (2006), A three dimensional radially anisotropic model of shear velocity in the whole mantle, *Geophysical Journal International*, *167*(1), 361–379, doi:10.1111/j.1365-246X.2006.03100.x.

Perry, H. K. C., A. M. Forte, and D. W. S. Eaton (2003), Upper-mantle thermochemical structure below North America from seismic-geodynamic flow models, *Geophysical Journal International*, *154*(2), 279–299, doi:10.1046/j.1365-246X.2003.01961.x.

Porritt, R. W., R. M. Allen, and F. F. Pollitz (2014), Seismic imaging east of the Rocky Mountains with USArray, *Earth and Planetary Science Letters*, *402*(0), 16–25, doi: 10.1016/j.epsl.2013.10.034.

Ritsema, J., and H.-J. van Heijst (2002), Constraints on the correlation of P- and S-wave velocity heterogeneity in the mantle from P, PP, PPP and PKP_{ab} traveltimes, *Geophysical Journal International*, *149*(2), 482–489, doi:10.1046/j.1365-246X.2002.01631.x.

Ritsema, J., H. J. van Heijst, and J. H. Woodhouse (2004), Global transition zone tomography, *Journal of Geophysical Research: Solid Earth*, *109*(B2), doi: 10.1029/2003JB002610.

Ritsema, J., A. Deuss, J. van Heijst, and W. J.H. (2011), S40RTS: a degree-40 shear-velocity model for the mantle from new Rayleigh wave dispersion, teleseismic traveltime and normal-mode splitting function measurements, *Geophysical Journal International*,

184(3), 1223–1236, doi:10.1111/j.1365-246X.2010.04884.x.

Ritzwoller, M., G. Masters, and F. Gilbert (1988), Constraining aspherical structure with low-degree interaction coefficients: Application to uncoupled multiplets, *Journal of Geophysical Research: Solid Earth*, *93*(B6), 6369–6396, doi:10.1029/JB093iB06p06369.

Robertson, G. S., and J. H. Woodhouse (1996), Ratio of relative S to P velocity heterogeneity in the lower mantle, *Journal of Geophysical Research: Solid Earth*, *101*(B9), 20,041–20,052, doi:10.1029/96JB01905.

Rosen, O., K. C. Condie, L. M. Natapov, and A. Nozhkin (1994), Archean and early proterozoic evolution of the siberian craton: A preliminary assessment, in *Archean Crustal Evolution*, vol. 11, chap. 10, pp. 411–459, Elsevier, doi:10.1016/S0166-2635(08)70228-7.

Rychert, C. A., K. M. Fischer, and S. Rondenay (2005), A sharp lithosphereasthenosphere boundary imaged beneath eastern North America, *Nature*, *436*, 542–545, doi:10.1038/nature03904.

Saad, Y., and M. H. Schultz (1986), GMRES: A generalized minimal residual algorithm for solving nonsymmetric linear systems, *SIAM Journal on Scientific and Statistical Computing*, *7*(3), 856–869, doi:10.1137/0907058.

Saltzer, R. L., R. D. van der Hilst, and H. Kárason (2001), Comparing P and S wave heterogeneity in the mantle, *Geophysical Research Letters*, *28*(7), 1335–1338, doi:10.1029/2000GL012339.

Schmidt, M. W., and S. Poli (1998), Experimentally based water budgets for dehydrating slabs and consequences for arc magma generation, *Earth and Planetary Science Letters*, *163*(1-4), 361–379, doi:10.1016/S0012-821X(98)00142-3.

812 Schuberth, B. S. A., C. Zaroli, and G. Nolet (2012), Synthetic seismograms for a synthetic
813 Earth: long-period P- and S-wave traveltime variations can be explained by tempera-
814 ture alone, *Geophysical Journal International*, *188*(3), 1393–1412, doi:10.1111/j.1365-
815 246X.2011.05333.x.

816 Sdrolias, M., W. R. Roest, and R. D. Müller (2004), An expression of Philippine Sea
817 plate rotation: the Parece Vela and Shikoku Basins, *Tectonophysics*, *394*(1-2), 69–86,
818 doi:10.1016/j.tecto.2004.07.061.

819 Shearer, P. M., K. M. Toy, and J. A. Orcutt (1988), Axi-symmetric earth models and
820 inner-core anisotropy, *Nature*, *333*, 228–232, doi:10.1038/333228a0.

821 Simmons, N. A., A. M. Forte, L. Boschi, and S. P. Grand (2010), GyPSuM: A joint
822 tomographic model of mantle density and seismic wave speeds, *Journal of Geophysical*
823 *Research: Solid Earth*, *115*, doi:10.1029/2010JB007631.

824 Su, W. J., and A. M. Dziewonski (1997), Simultaneous inversion for 3-D variations in
825 shear and bulk velocity in the mantle, *Physics of the Earth and Planetary Interiors*,
826 *100*(1-4), 135–156, doi:10.1016/S0031-9201(96)03236-0.

827 Tapponnier, P., G. Peltzer, A. Y. L. Dain, R. Armijo, and P. Cobbold (1982), Propagat-
828 ing extrusion tectonics in Asia: New insights from simple experiments with plasticine,
829 *Geology*, *10*(12), 611–616.

830 Thybo, H., and E. Perchuć (1997), The seismic 8° discontinuity and partial melting in
831 continental mantle, *Science*, *275*(5306), 1626–1629, doi:10.1126/science.275.5306.1626.

832 Trampert, J., F. Deschamps, J. Resovsky, and D. Yuen (2004), Probabilistic tomography
833 maps chemical heterogeneities throughout the lower mantle, *Science*, *306*(5697), 853–
834 856, doi:10.1126/science.1101996.

van der Hilst, R. D., S. Widiyantoro, and E. R. Engdahl (1997), Evidence for deep mantle circulation from global tomography, *Nature*, *386*, 578–584, doi:10.1038/386578a0.

van Keken, P. E. (2003), The structure and dynamics of the mantle wedge, *Earth and Planetary Science Letters*, *215*(3-4), 323–338, doi:10.1016/S0012-821X(03)00460-6.

Visser, K., J. Trampert, and B. L. N. Kennett (2008), Global anisotropic phase velocity maps for higher mode Love and Rayleigh waves, *Geophysical Journal International*, *172*(3), 1016–1032, doi:10.1111/j.1365-246X.2007.03685.x.

Wang, Z., and F. A. Dahlen (1994), JWKB surface-wave seismograms on a laterally heterogeneous earth, *Geophysical Journal International*, *119*, 381–401, doi:0.1111/j.1365-246X.1994.tb00130.x.

Yuan, H., B. A. Romanowicz, K. Fischer, and D. Abt (2011), 3-D shear wave radially and azimuthally anisotropic velocity model of the North American upper mantle, *Geophysical Journal International*, *184*(3), 1237–1260, doi:10.1111/j.1365-246X.2010.04901.x.

Table 1. Surface wave phases used in this study

Author	Phase and dominant period	Number of measurements
[Ekström, 2011]	R0 25-250s	1022706
	L0 25-250s	342261
[Visser et al., 2008]	R1 35-172s	396432
	R2 35-149s	364140
	R3 35-87s	253143
	R4 35-61s	159448
	R5 35-56s	114037
	R6 35-50s	71652
	L1 35-176s	331168
	L2 35-115s	250315
	L3 35-78s	154160
	L4 35-62s	81592
	L5 35-56s	42756

Table 2. Body wave phases used in this study

Author	Phase	Number of measurements
[Antolik et al., 2003]	P	621892
[Ritsema and van Heijst, 2002]	pPP	12054
	pP	20780
	PP	167144
	PPP	15060
	$pPPP$	2089
[Ritsema et al., 2011]	S	144696
	SKS	31971
	$SKKS$	8727
	ScS	8475
	$ScSScS$	13505
	$ScSScSScS$	7983

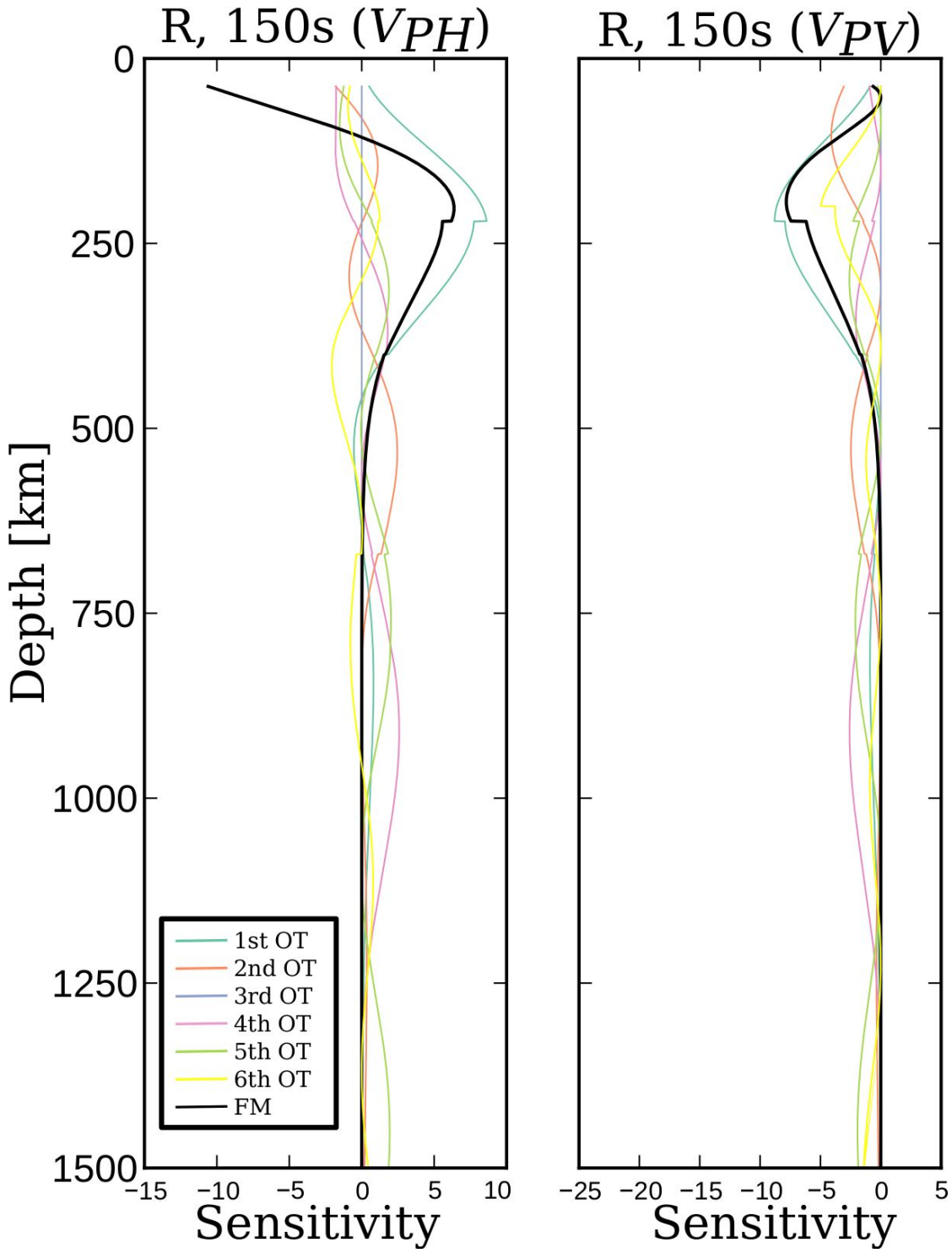

Figure 1. Depth sensitivity kernels to horizontal (V_{PH}) and vertical (V_{PV}) compressional wave velocity structure for a 150s period Rayleigh wave. The fundamental mode is drawn in black and higher overtones are shown in color. Love waves are completely insensitive to compressional wave velocity.

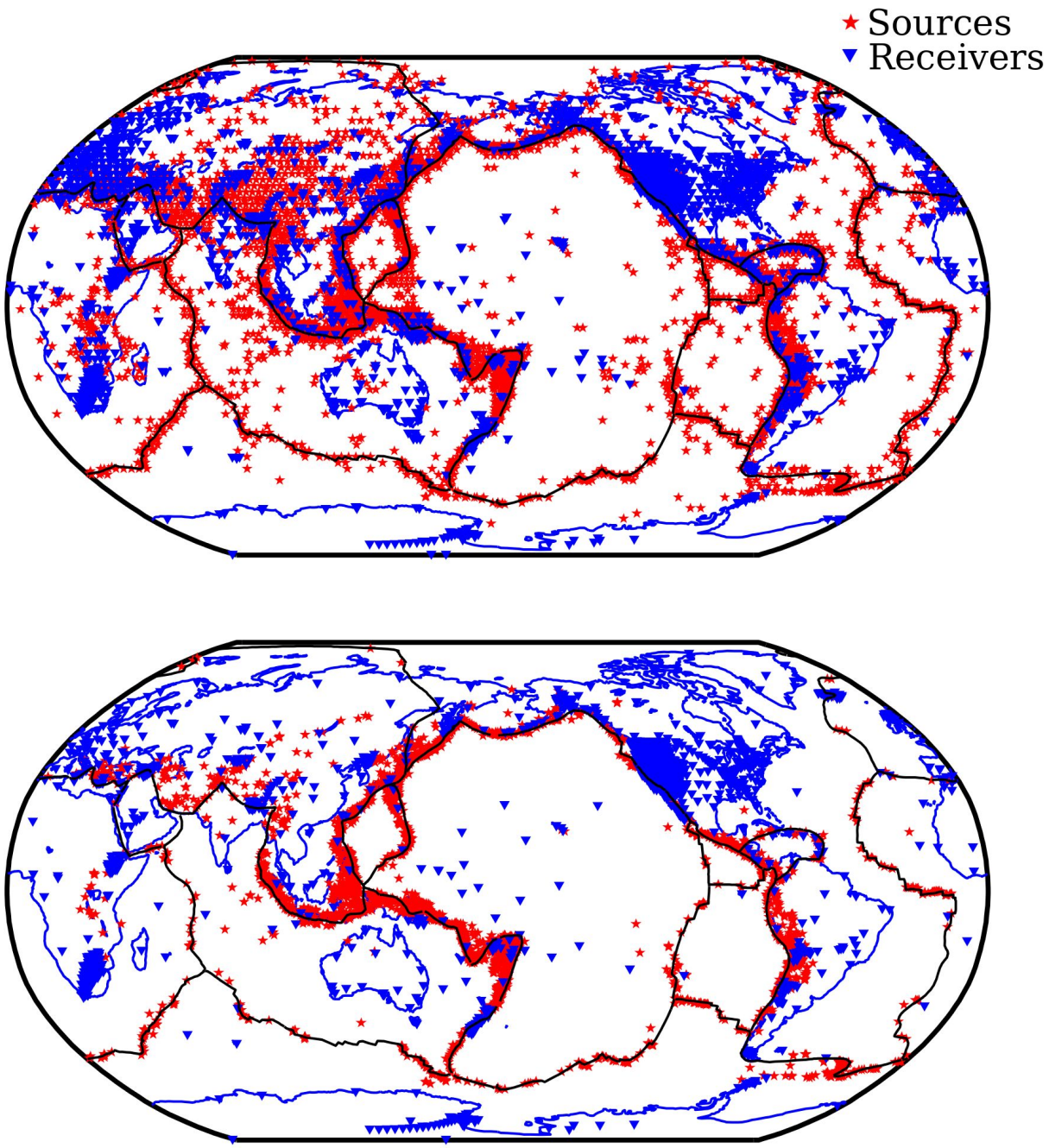

Figure 2. Distribution of sources (red) and receivers (green) used in this study for P (top) and S (bottom) body wave phases.

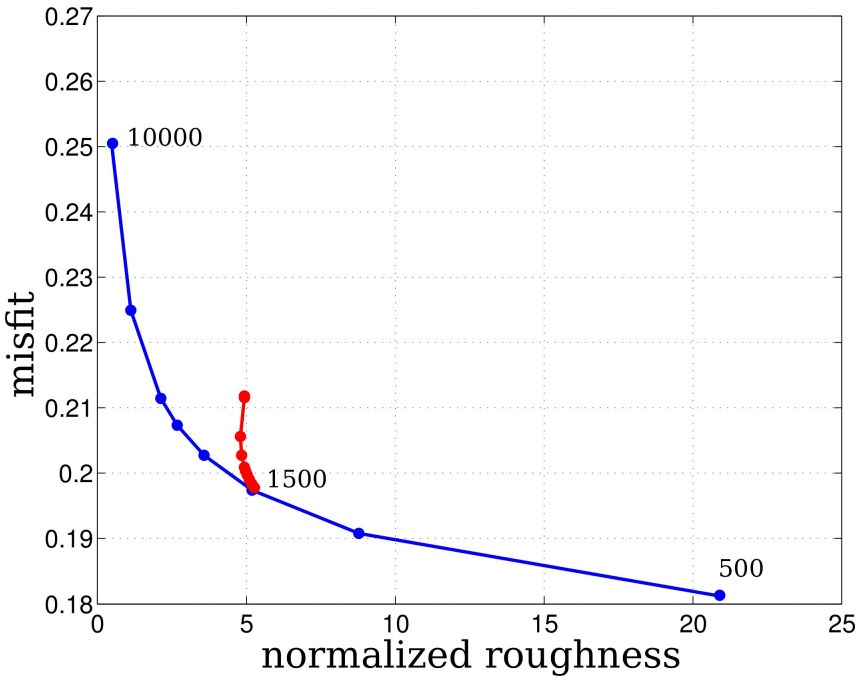

Figure 3. L-curve (blue) showing the performed analysis to select the most appropriate weight of the roughness parameter. The numbers within the plot indicate two end-member tested values and the value we select (1500) for our model $SPani_{test}$. The same analysis, repeated by only changing the weight of mineral physics scaling relationship between V_S and V_P, is shown in red.

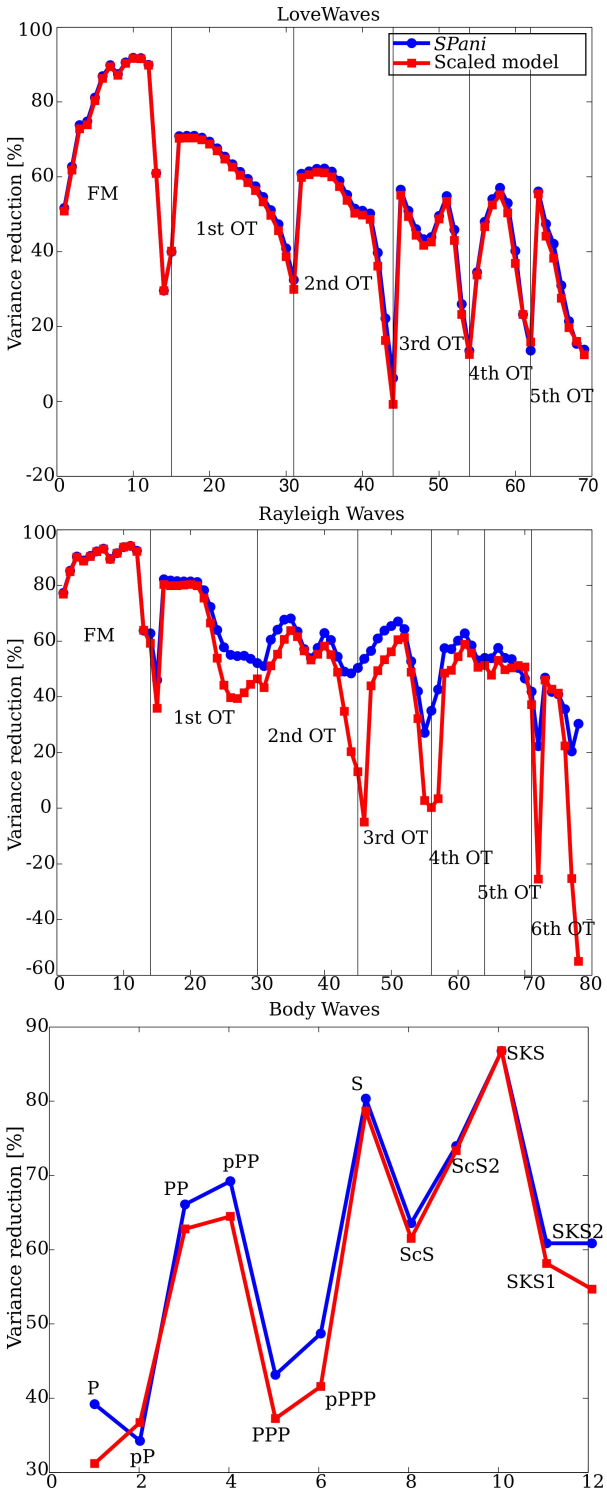

Figure 4. Variance reduction for all the subset of data: Love waves (top), Rayleigh waves (middle) and body waves (bottom). Variance reduction of our final model *SPani* is in blue, variance reduction of a model whose V_P component is perfectly scaled to its V_S component is shown in red.

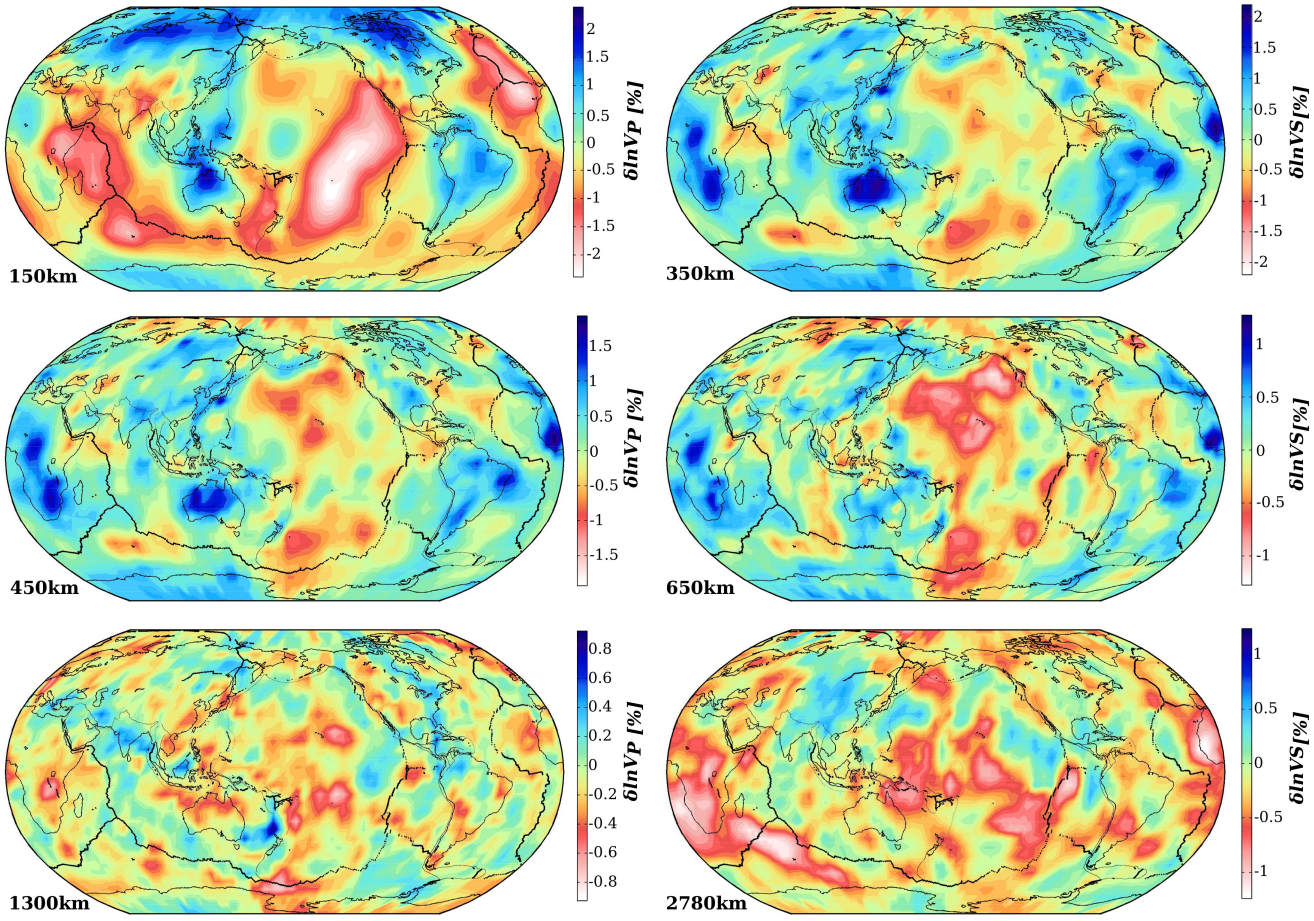

Figure 5. Isotropic V_P relative variations in percent at different depths for $SPani_{test}$. V_S structure is very similar to our preferred model $SPani$.

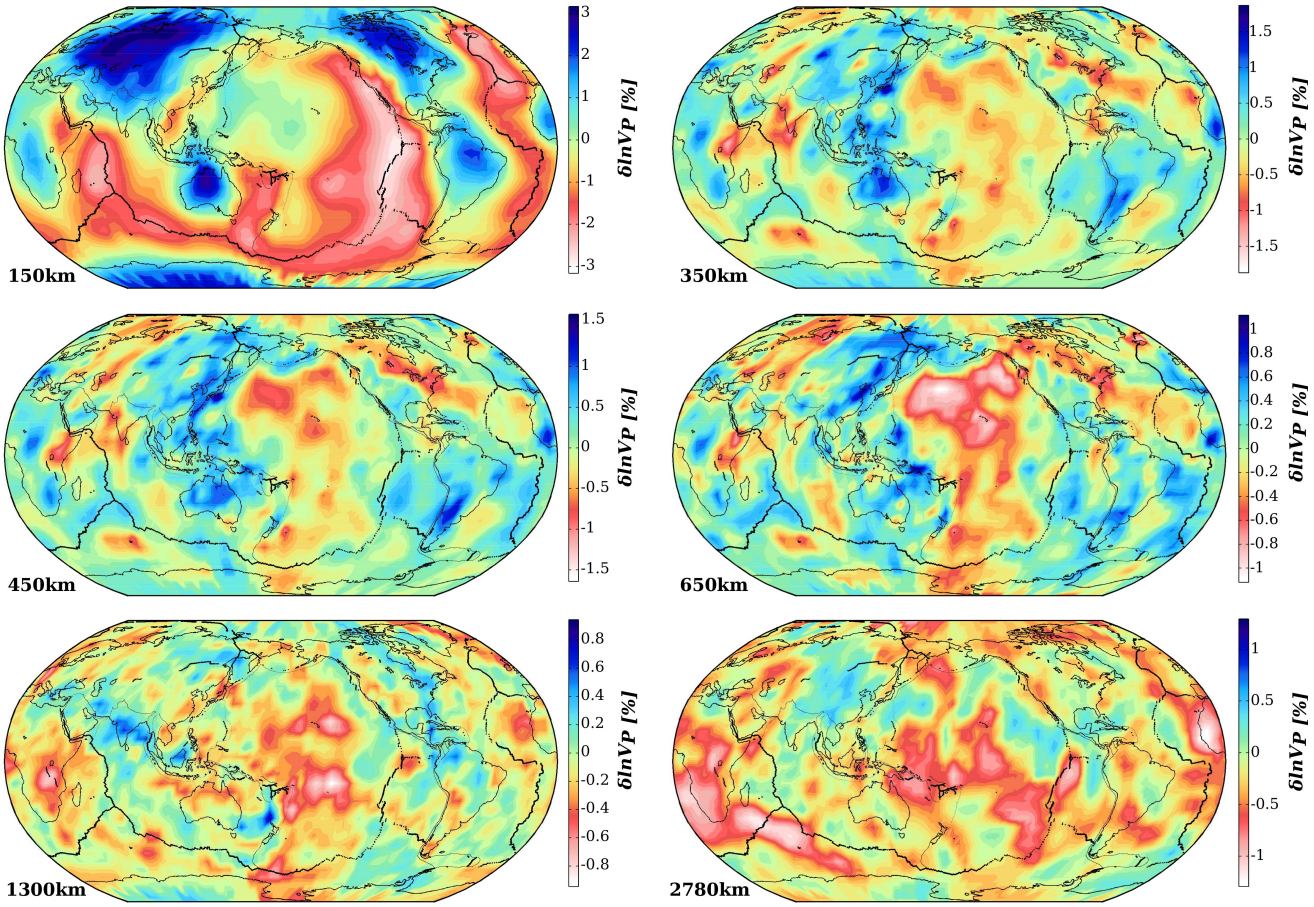

Figure 6. Isotropic V_P relative variations at different depths for our preferred model *SPani*.

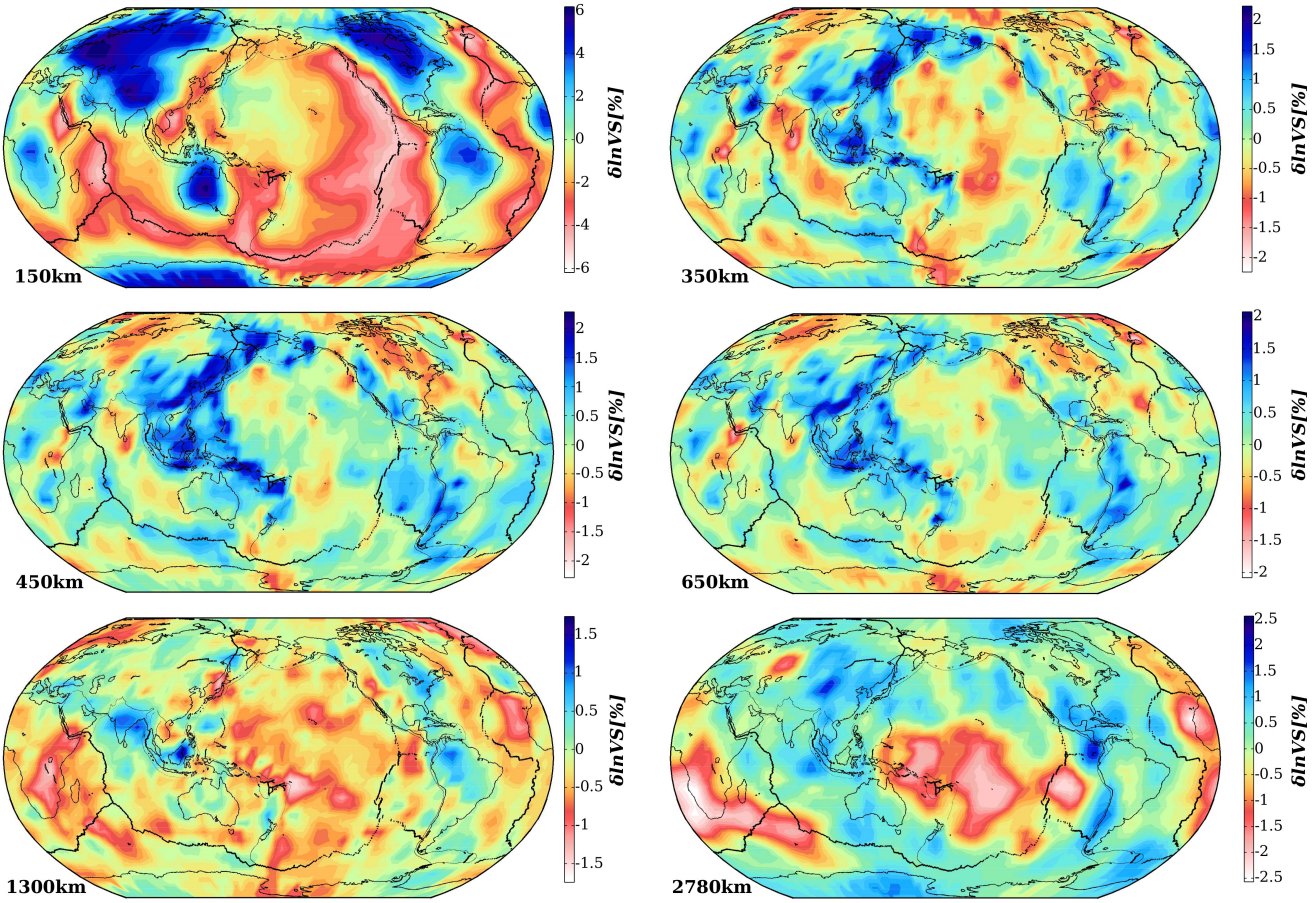

Figure 7. Isotropic V_S relative variation at different depths for our preferred model *SPani*.

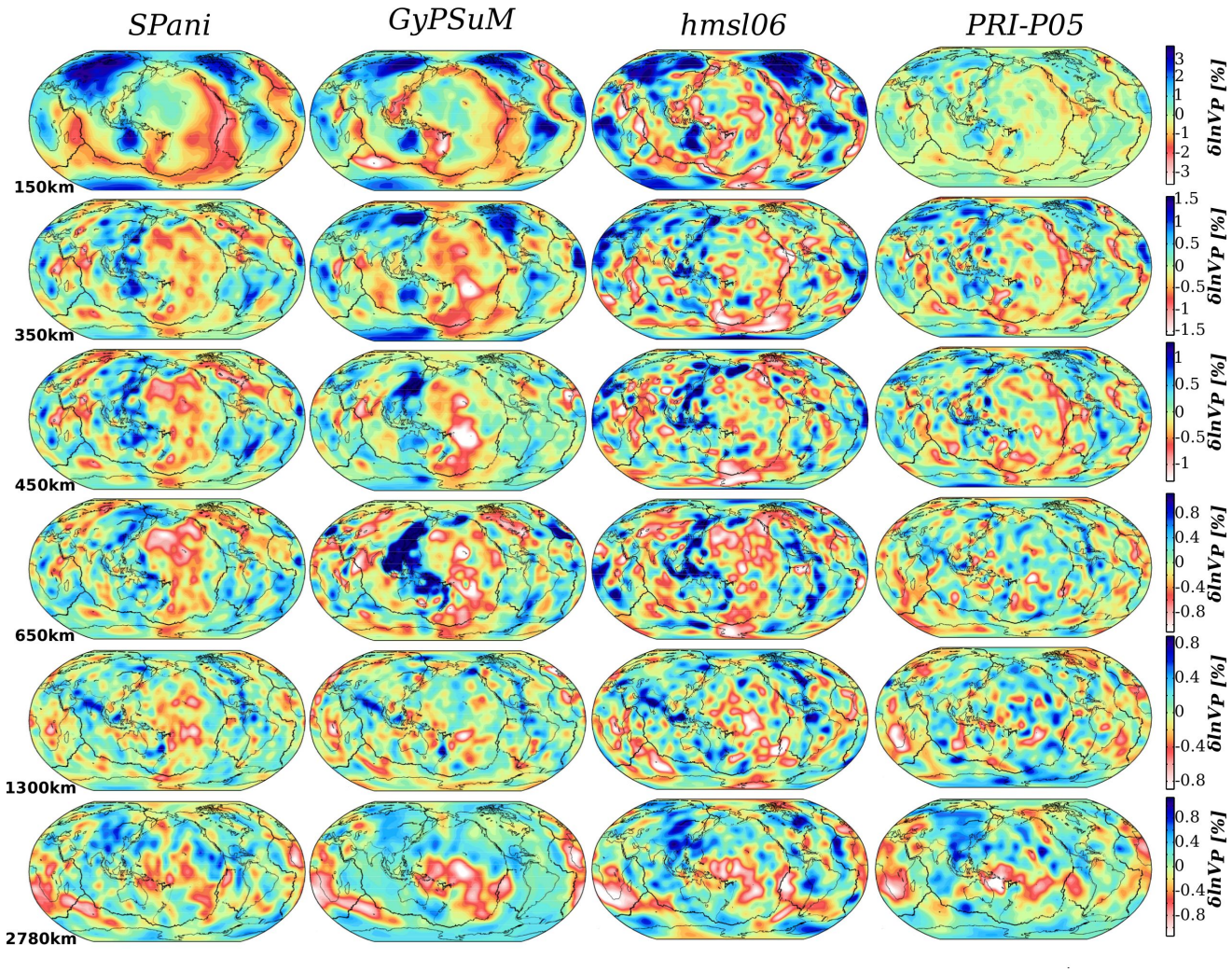

Figure 8. Isotropic V_P relative variations in percent at different depths for four global tomographic models *SPani*, *GyPSuM* [*Simmons et al.*, 2010], *hmsl06* [*Houser et al.*, 2008] and *PRI-P05* [*Montelli et al.*, 2004]. Models are resampled in spherical harmonics from degree 1 to 32.

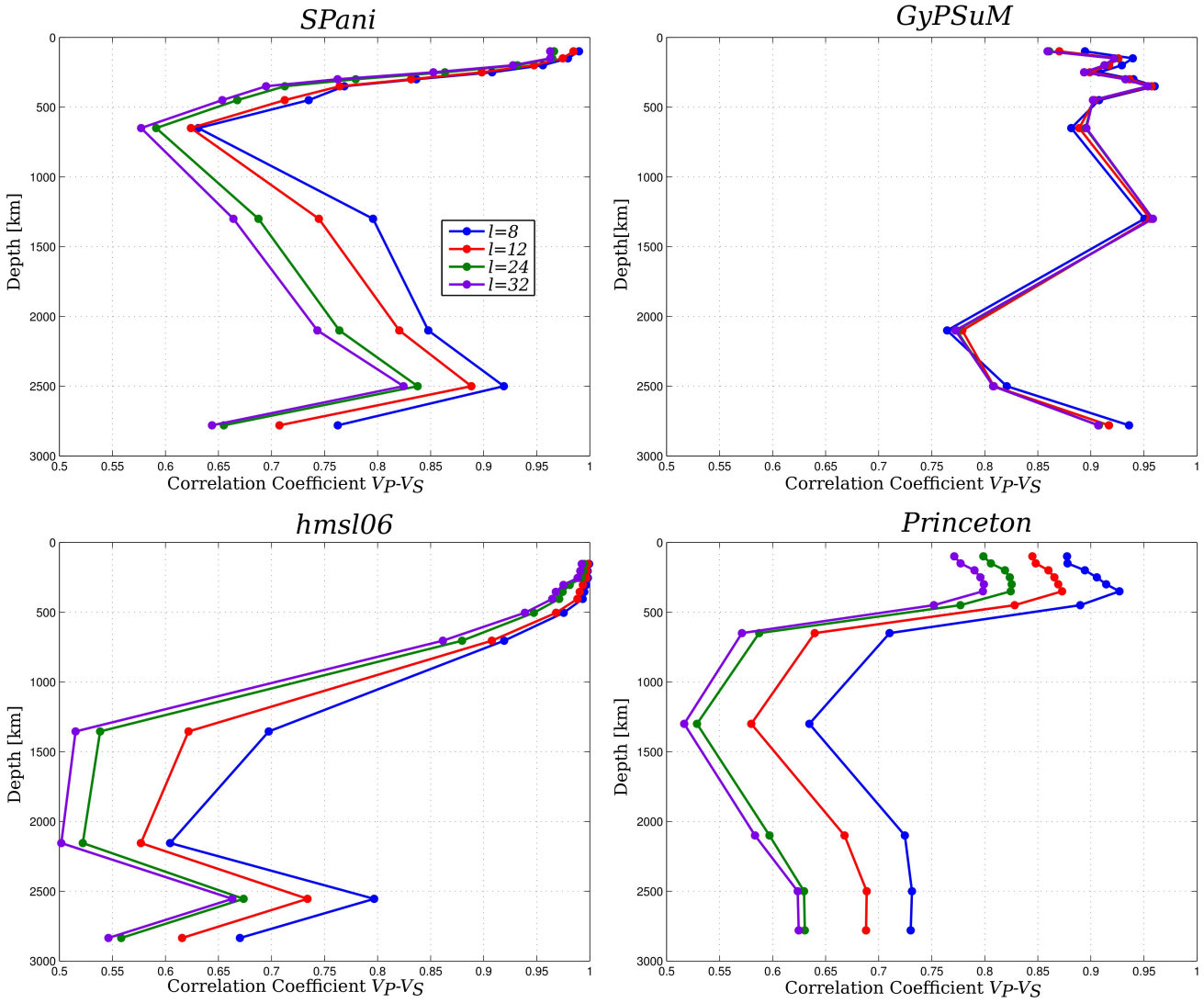

Figure 9. Pearson correlation coefficient between the V_P and the V_S component of the analyzed models as a function of depth.

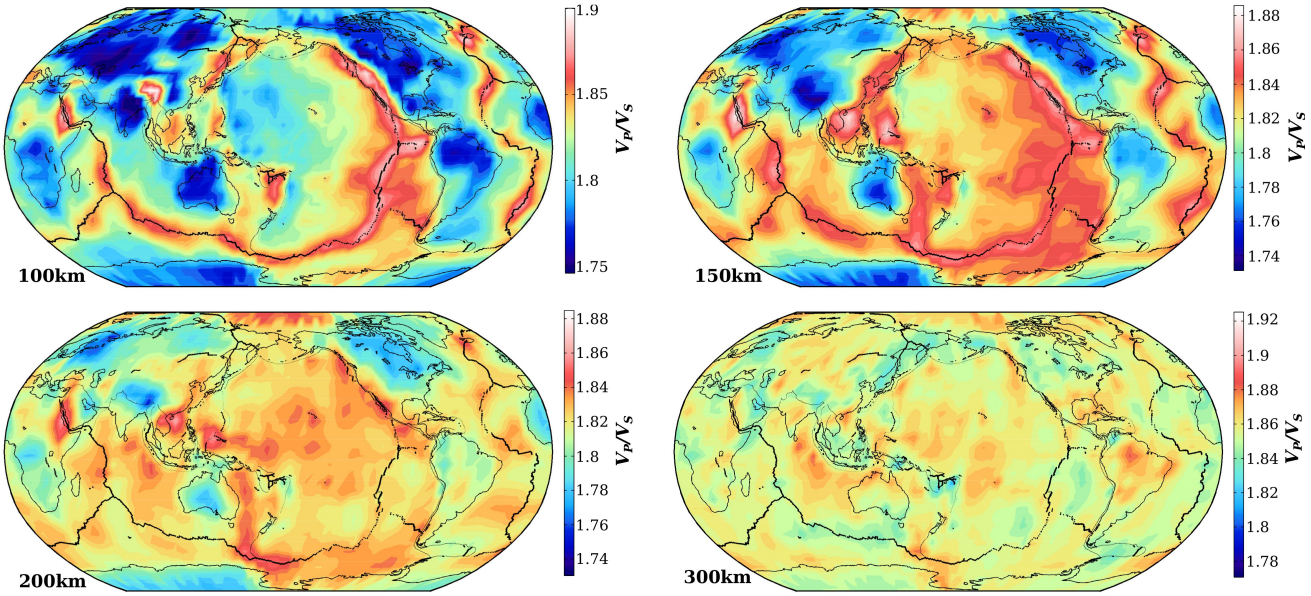

Figure 10. V_P/V_S ratio of *SPani* at four selected upper mantle depths. Mid oceanic ridges and sub-continental regions show high and low values, respectively, in the top part of the upper mantle. Comparable, and even slightly higher, V_P/V_S ratio to mid-oceanic ridges are observed in the Western Pacific between 150 km and 200 km depth.

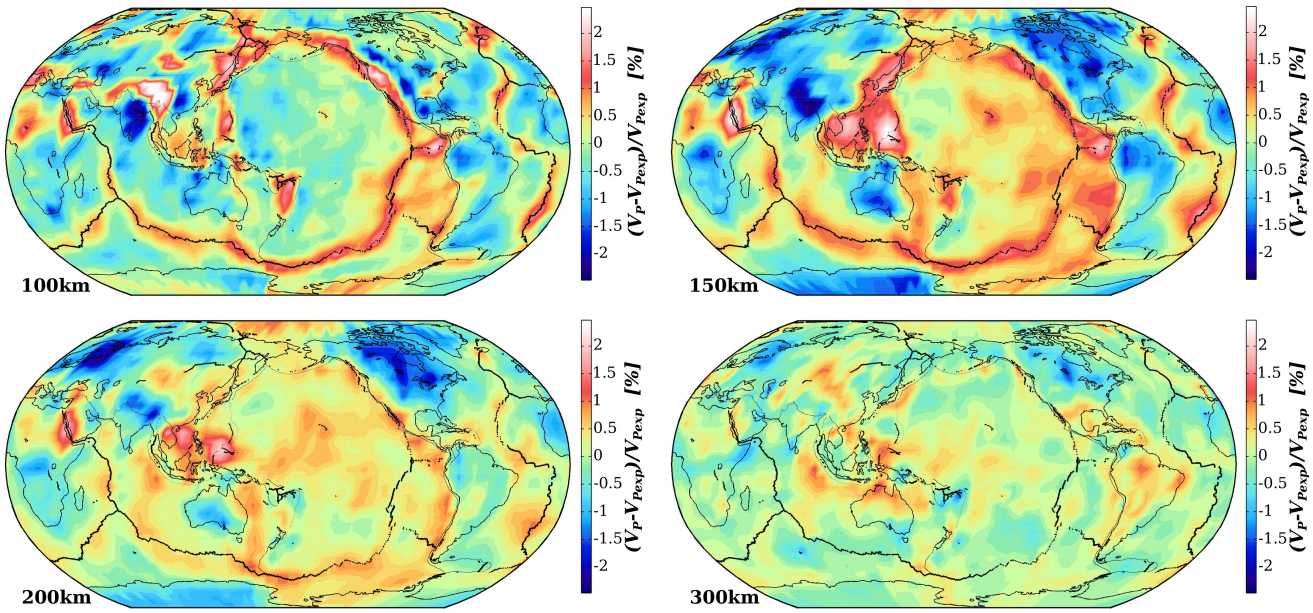

Figure 11. Percentage difference between V_P (and V_P/V_S ratio) of *SPani* and the expected V_P (and V_P/V_S) ratio if our scaling between V_P ands V_S is rigorously applied. Note the strong positive anomalies in the tectonic plates along the Western Pacific margin and negative anomalies in continental regions.

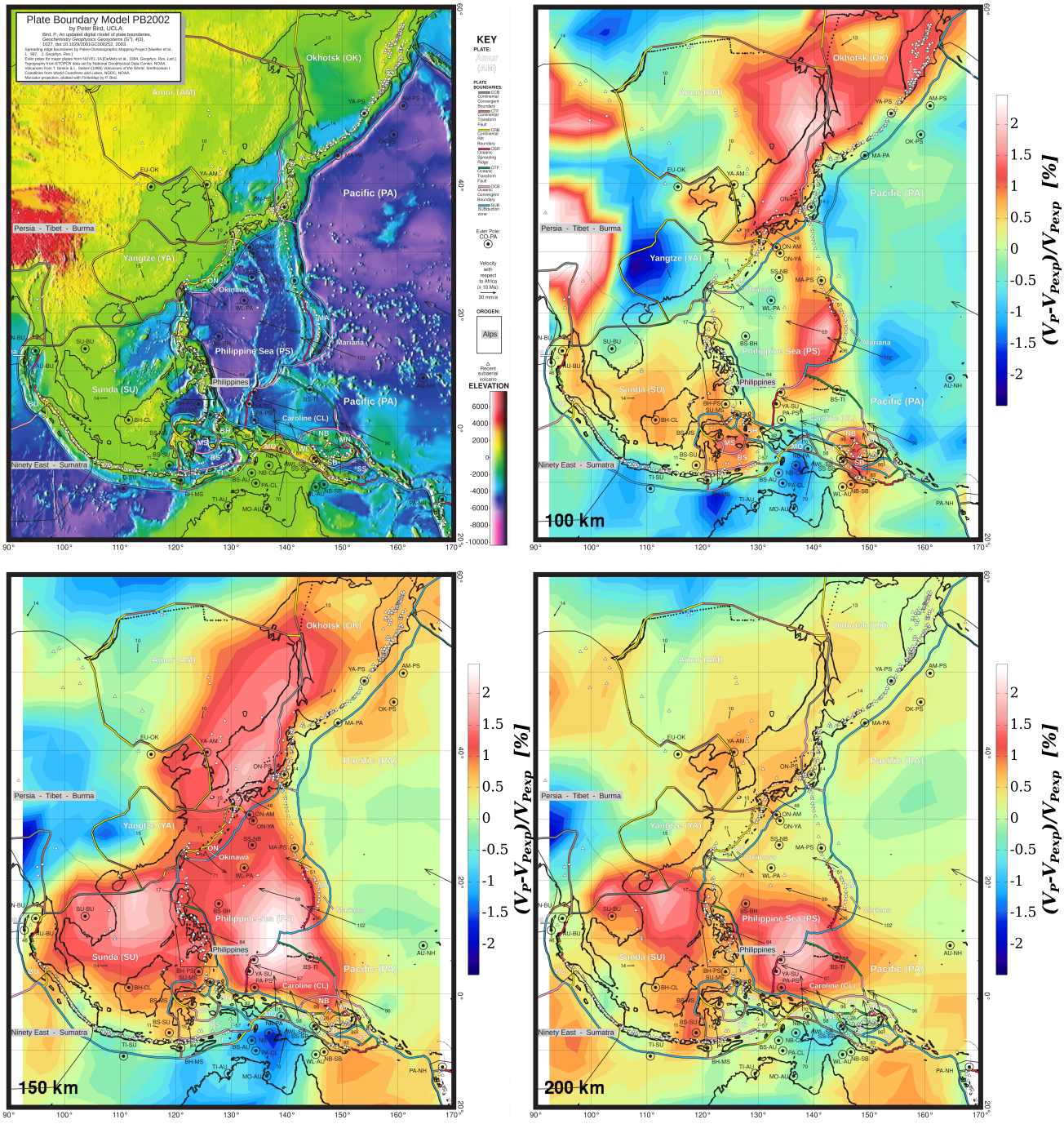

Figure 12. Detail of the V_P/V_S anomaly in the Western Pacific at 100 km (top right), 150 km (bottom left), and 200 km depth (bottom right). On top-left panel, plate boundary model PB2002 *Bird* [2003] and topography is shown as reference.

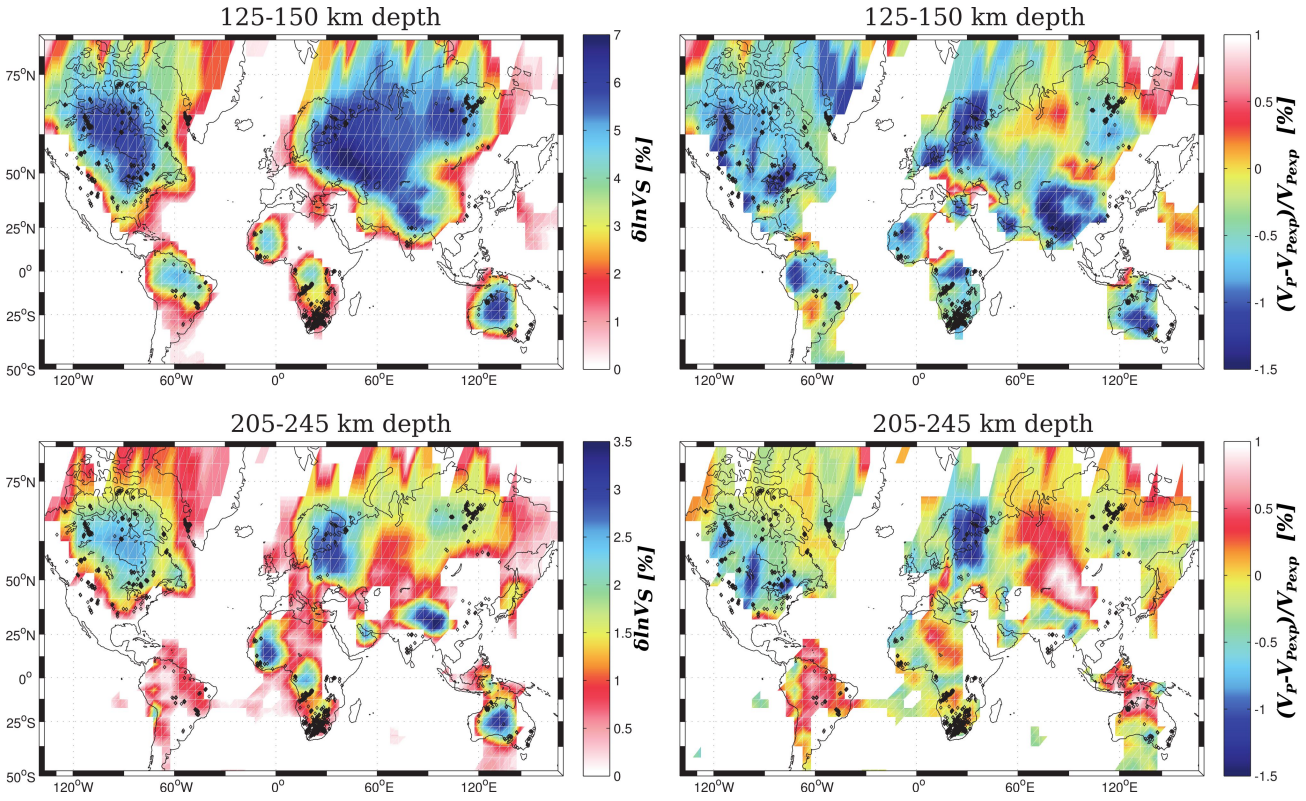

Figure 13. *SPani* V_S (left panels) and $V_P - V_{Pexp}$ anomalies (right panels) in regions that have faster than average V_S at $\sim$ 135 km and $\sim$ 220 km depth. Kimberlite from Consorem database [*Faure*, 2006] are also shown. South hemisphere region is not shown in this map.